

**Radio & Optical Interferometry:
Basic Observing Techniques and Data Analysis**

*To be published by Springer in Volume 2 of
Planets, Stars, & Stellar Systems*

J.D. Monnier¹ & R.J. Allen²

ABSTRACT

Astronomers usually need the highest angular resolution possible when observing celestial objects, but the blurring effect of diffraction imposes a fundamental limit on the image quality from any single telescope. Interferometry allows light collected at widely-separated telescopes to be combined in order to synthesize an aperture much larger than an individual telescope thereby improving angular resolution by orders of magnitude. Because diffraction has the largest effect for long wavelengths, radio and millimeter wave astronomers depend on interferometry to achieve image quality on par with conventional large-aperture visible and infrared telescopes. Interferometers at visible and infrared wavelengths extend angular resolution below the milli-arcsecond level to open up unique research areas in imaging stellar surfaces and circumstellar environments.

In this chapter the basic principles of interferometry are reviewed with an emphasis on the common features for radio and optical observing. While many techniques are common to interferometers of all wavelengths, crucial differences are identified that will help new practitioners to avoid unnecessary confusion and common pitfalls. The concepts essential for writing observing proposals and for planning observations are described, depending on the science wavelength, the angular resolution, and the field of view required. Atmospheric and ionospheric turbulence degrades the longest-baseline observations by significantly reducing the stability of interference fringes. Such instabilities represent a persistent challenge, and the basic techniques of phase-referencing and phase closure have been developed to deal with them. Synthesis imaging with large observing datasets has become a routine and straightforward process at radio observatories, but remains challenging for optical facilities. In this context the commonly-used image reconstruction algorithms CLEAN and MEM are presented. Lastly, a concise overview of current facilities is included as an appendix.

¹monnier@umich.edu; Univ. Michigan Astronomy Dept., 941 Dennison Bldg, Ann Arbor, MI 48109-1090, USA.

²rjallen@stsci.edu; Space Telescope Science Institute, 3700 San Martin Drive, Baltimore, MD 21218, USA

1. Interferometry in Astronomy

1.1. Introduction

The technique of interferometry is an indispensable tool for modern astronomy. Typically the telescope diameter D limits the angular resolution for an imaging system to $\Theta \approx \frac{\lambda}{D}$ owing to diffraction, but interferometry allows the achievement of angular resolutions $\Theta \approx \frac{\lambda}{B}$ where the baseline B is set by the distance between telescopes. Interferometry has permitted the angular resolution at radio wavelengths to initially reach, and now to significantly surpass, the resolution available with both ground- and space-based optical telescopes. Indeed, radio astronomers routinely create high-quality images with high sensitivity, high angular resolution, and a large field-of-view using arrays of telescopes such as the Very Large Array (VLA), the Combined Array for Research in Millimeter-wave Astronomy (CARMA), and now the Atacama Large Millimeter Array (ALMA). Interferometer arrays are now the instruments of choice for imaging the wide range of spatial structures found both for Galactic and for extragalactic targets at radio wavelengths.

At optical wavelengths, interferometry can improve the angular resolution down to the milli-arcsecond level, an order-of-magnitude better than even the Hubble Space Telescope. While atmospheric turbulence limits the sensitivity much more dramatically than for the radio, optical interferometers can nevertheless measure the angular sizes of tens of thousands of nearby Galactic objects and even a growing sample of distant Active Galactic Nuclei (AGN). Recently, optical synthesis imaging of complex objects has been demonstrated with modern arrays of 4–6 telescopes, producing exciting results and opening new avenues for research.

Both radio and optical interferometers also excel at precision astrometry, with the potential for *micro-arcsecond*-level precision for some applications. Currently, it is ground-based radio interferometry (e.g. the VLBA) that provides the highest astrometric performance, although ground-based near-IR interferometers are improving and measure different astronomical phenomena.

This chapter will provide an overview of interferometry theory and present some practical guidelines for planning observations and for carrying out data analysis at the premier ground-based radio and optical interferometer facilities currently available for research in astronomy. In this chapter, the term “radio” will be used as a shorthand for the whole class of systems from sub-mm to decametric wavelengths which usually employ coherent high-frequency signal amplification, superheterodyne signal conversion, and digital signal processing, although detailed instrumentation can vary substantially. Likewise, the term “optical” generally describes systems employing direct detection, i.e. the direct combination of the signals from each collector without amplification or mixing with locally-generated signals¹.

¹It should be emphasized, however, that this distinction is somewhat artificial; the first meter-wave radio interferometers \approx 65 years ago were simple Michelson adding interferometers employing direct detection without coherent high-frequency signal amplification. At the other extreme, superheterodyne systems are currently routinely used at wavelengths as short as $10\mu\text{m}$, such as the UC Berkeley ISI facility.

Historically, radio and optical interferometry have usually been discussed and reviewed independently from each other, leaving the student with the impression that there is something fundamentally different between the two regimes of wavelength. Here a different approach is taken, presenting a unified and more wavelength-independent view of interferometry, nonetheless noting important practical differences along the way. This perspective will demystify some of the differing terminology and techniques in a more natural way, and hopefully will be more approachable for a broad readership seeking general knowledge. For a more much detailed treatment of radio interferometry specifically, refer to the classic text by Thompson et al. (2001) and the series of lectures in the NRAO Summer School on Synthesis Imaging (e.g. Taylor et al. 1999). Optical interferometry basics have been covered in individual reviews by Quirrenbach (2001) and by Monnier (2003), and a useful collection of course notes can be found in the NASA-Michelson Course Notes (Lawson 2000) and ESO-VLTI summer school proceedings (Malbet & Perrin 2007). Recently, a few textbooks have been published on the topic of optical interferometry specifically, including Labeyrie et al. (2006), Glindemann (2010), and Saha (2011). Further technical details can also be found in Chapters 7 and 13 of the first volume in this series.

This chapter begins with a brief history of interferometry and its scientific impact on astronomy, a basic scientific context for newcomers that illustrates why the need for better angular resolution has been and continues to be one of the most important drivers for technical innovation in astronomy.

1.2. Scientific impact

Using interferometers in a synthesis imaging array allows designers to decouple the diffraction-limited angular resolution of a telescope (which improves linearly with the telescope size) from its collecting area (which, for a filled aperture, grows quadratically with the size). In the middle of the 20th century, radio astronomers faced a challenge in their new science; the newly-discovered “radio stars” were bright enough to be observed with radio telescopes of modest collecting area, but the resolution of conventional “filled aperture” reflecting telescopes was woefully inadequate (by one or more orders of magnitude) to measure the positions and angular sizes of these enigmatic new cosmological objects with a precision sufficient to permit an identification with an optical object. Thus separated-element interferometry, although first applied in astronomy at optical wavelengths (Michelson & Pease 1921), began to be applied in the radio with revolutionary results.

At radio wavelengths, the epoch of rapid technological development began more than 50 years ago, and now interferometry is the “workhorse” technique of choice for most radio astronomers in the world. A steady stream of exciting new results has flowed from these instruments even until today, and a complete census of the major discoveries to date would be very lengthy indeed. Here, our attention is focussed on the earliest historical discoveries that *required* radio interferometers, and we have listed our nominations in Table 1. In Figure 1a, the spectacular image of radio jets in quasar 3C175 by the VLA is shown to illustrate the high-fidelity imaging that is possible using

today’s radio facilities.

Modern long-baseline optical interferometry started approximately 30 years after radio interferometry, following the pioneering experiments and important scientific results with the Narrabri intensity interferometry (e.g., Hanbury Brown et al. 1974) and the heterodyne work of the Townes’ group at Berkeley (Johnson et al. 1974). The first successful direct interference of stellar light beams from separated telescopes was achieved in 1974 (Labeyrie 1975) and this was followed by about twenty years of two-telescope (i.e., single baseline) experiments which measured the angular diameters of a variety of objects for the first time. The first imaging arrays with more than two telescopes were constructed in the 1990s, and the COAST interferometer was first to make a true optical synthesis image using techniques familiar to radio astronomers (Baldwin et al. 1996). Keck and VLT interferometers both include 8-m class telescopes, making them the most sensitive facilities in the world. Recently, the CHARA array has produced a large number of new images in the infrared using combinations of 4 telescopes simultaneously. Table 1 lists a few major scientific accomplishments in the history of optical interferometry showing the diversity of contributions in many areas of stellar astronomy and even recent extragalactic observations of active galactic nuclei. With technical and algorithm advances, model-independent imaging has become more powerful and a state-of-the-art image from the CHARA array is presented in Figure 1b, showing the surface of the rapidly rotating star Alderamin.

2. Interferometry in theory and practice

2.1. Introduction

The most basic interferometer used in observational astronomy consists of two telescopes configured to observe the same object and connected together as a Michelson interferometer. Photons collected at each telescope are brought together to a central location and combined coherently at the “correlator” (radio term) or the “combiner” (optical term). For wavelengths longer than ~ 0.2 millimeters, the free-space electric field is usually converted into cabled electrical signals and coherently amplified at the focus of each telescope. The celestial signal is then mixed with a local oscillator signal sent to both telescopes from a central location, and the difference frequency transmitted in cables back to the centrally-located correlator. For shorter wavelengths, cable losses increase, and signal transmission moves eventually into free space in a more “optical” mode, using mirrors and long-distance transmission of light beams in (sometimes evacuated) pipes.

Depending on the geometry, the light from an astronomical object will in general be received at one telescope before it arrives at the other. If the fractional signal bandwidth $\Delta\nu$ is very narrow (either because of the intrinsic emission properties of the source, e.g. a spectral line, or because of imposed bandwidth limitations in amplifiers and/or filters), then the signal has a high degree of “temporal coherence”, which is to say that the wave packet describing all the photons in the signal is extended in time by $\tau \approx 1/\Delta\nu$ seconds. Expressing the bandwidth in terms of wavelength,

Table 1. Some historically-important astronomical results made possible by interferometry

Astronomical Result	Date	Facility	References ^a
<i>Radio Interferometry^b</i>			
Solar radio emission from sunspots	1945-46	Australia, Sea cliff interferometer	R1
First Radio Galaxies NGC 4486 & NGC 5128	1948	New Zealand, Sea cliff interferometer	R2
Identification of Cygnus A	1951-53	Cambridge, Würzburg antennas	R3
Cygnus A double structure	1953	Jodrell Bank, Intensity interferometer	R4
AGN superluminal motions	1971	Haystack-Goldstone VLBI	R5
Dark matter in spiral galaxies	1972-78	Caltech interferometer, Westerbork SRT	R6
Spiral arm structure & kinematics	1973-80	Westerbork SRT	R7
Compact source in Galactic center	1974	NRAO Interferometer	R8
Gravitational lenses	1979	Jodrell Bank Mk1 + Mk2 VLBI	R9
NGC 4258 black hole	1995	NRAO VLBA	R10
<i>Optical Interferometry</i>			
Physical diameters of hot stars	1974	Narrabri Intensity Interferometer	O1
Empirical effective temperature scale for giants	1987	I2T/CERGA	O2
Survey of IR Dust Shells	1994	ISI	O3
Geometry of Be star disks	1997	Mark III	O4
Near-IR Sizes of YSO disks	2001	IOTA	O5
Pulsating Cepheid ζ Gem	2001	PTI	O6
Crystalline silicates in inner YSO disks	2004	VLTI	O7
Vega is a rapid rotator	2006	NPOI	O8
Imaging gravity-darkening on Altair	2007	CHARA	O9
Near-IR sizes of AGN	2009	Keck-I	O10

^aReferences: R1: Pawsey et al. (1946); McCready et al. (1947). R2: Bolton et al. (1949). R3: Smith (1951); Baade & Minkowski (1954). R4: Jennison & Das Gupta (1953). R5: Whitney et al. (1971); Cohen et al. (1971). R6: Rogstad & Shostak (1972); Bosma (1981a,b). R7: Allen et al. (1973); Rots & Shane (1975); Rots (1975); Visser (1980b,a). R8: Goss et al. (2003). R9: Porcas et al. (1979); Walsh et al. (1979). R10: Miyoshi et al. (1995). O1: Hanbury Brown et al. (1974). O2: di Benedetto & Rabbia (1987). O3: Danchi et al. (1994). O4: Quirrenbach et al. (1997). O5: Millan-Gabet et al. (2001). O6: Lane et al. (2000). O7: van Boekel et al. (2004). O8: Peterson et al. (2006). O9: Monnier et al. (2007). O10: Kishimoto et al. (2009).

^bRadio list in part from Wilkinson et al. (2004) and R.D. Ekers (2010, priv. comm.), with additions by one of the authors (RJA). Historical material prior to 1954 is also from W.M. Goss (2011, private communication) and Sullivan (2009).

$\Delta\nu = (c/\lambda_0^2) \cdot \Delta\lambda$ where λ_0 is the band center and c is the speed of light. The coherence time is then $\tau = (1/c) \cdot (\lambda_0^2/\Delta\lambda)$, and $c \cdot \tau$ is a scale size of the wave packet called the *coherence length*, $L_c = c \cdot \tau = \lambda_0^2/\Delta\lambda$, (e.g. Hecht 2002, Ch. 7). If the path difference between the two collectors in an interferometer is a significant fraction of L_c , an additional time delay must be introduced, otherwise the fringe amplitude will decrease or even disappear. For ground-based systems, the geometry is continually changing for all directions in the sky (except in the directions to the equatorial poles), requiring a continually-changing additional delay to maintain the temporal coherence. The special location on the sky where the adjusted time delay is matched perfectly is often called the “phase center” or point of zero optical path delay (OPD), although such a condition actually defines the locus of a plane passing through the mid-point between the collectors and perpendicular to the baseline, and cutting the celestial sphere in a great circle. Since the telescope optics usually limits the field of view to only a tiny portion of this great circle, adjusting the phase center is the equivalent of “pointing” the interferometer at a given object within that field of view.

The final step is to interfere the two beams to measure the *spatial coherence* (often called the mutual coherence) of the electric field as sampled by the two telescopes. If the object observed is much smaller than the angular resolution of the interferometer, then interference is complete and one observes 100% coherence at the correlator/combiner. However, objects that are *resolved* (i.e., much larger than the angular resolution of the interferometer) will show less coherence due to the fact that different patches of emission on the object do not interfere at the same time through our system. Figure 2 shows two simple cases of an interferometer as a Young’s two-slit experiment to illustrate basic principles. At the left, the interferometer is made up of two slits and the response for a monochromatic point source (i.e., incoming plane waves) is shown. The result should be familiar: an interference fringe modulating the intensity from 100% to 0% with a periodicity that corresponds to a fringe spacing of $\frac{\lambda}{B}$ on the sky. Next to this panel is shown an example of two equal-brightness point sources separated by $\frac{1}{2} \frac{\lambda}{B}$, half the fringe spacing. The location of constructive interference for one point coincides with the location of destructive interference for the other source. Since the two sources are mutually incoherent, the superposition of the two fringe results in an even light distribution, i.e. no fringe at all! In optical interferometry language, the first example fringe has a fringe contrast (or visibility) of 1 while the second example fringe has a visibility of 0.

Figure 3 contains a schematic of a basic interferometer as typically realized for both radio and optical configurations. While instrumental details vary immensely in how one transmits and interferes the signals for radio, millimeter, infrared, and visible-light interferometers, the basic principles are the same. The foundational theory common to all interferometers will be introduced next.

2.2. Interferometry in theory

The fundamental equation of interferometry is typically derived by introducing the van-Cittert Zernike Theorem and a complete treatment can be found in Chapter 3 of the book by Thompson et al.

(2001). Here the main result will be presented without proof, beginning by defining an interferometric observable called the *complex visibility*, $\tilde{\mathcal{V}}$. The visibility can be derived from the intensity distribution on the sky $I(\vec{\sigma})$ using a given interferometer baseline \vec{B} (which is the separation vector between two telescopes) and the observing wavelength λ :

$$\tilde{\mathcal{V}} = |\mathcal{V}|e^{i\phi_{\mathcal{V}}} = \int_{\text{sky}} A_N(\vec{\sigma})I(\vec{\sigma})e^{-\frac{2\pi i}{\lambda}\vec{B}\cdot\vec{\sigma}}d\Omega \quad (1)$$

Here, the $\vec{\sigma}$ represents the vector pointing from the center of the field-of-view (called the “phase center”) to a given location on the celestial sphere using local (East, North) equatorial coordinates and the telescope separation vector \vec{B} also using east and north coordinates. The modulus of the complex visibility $|\mathcal{V}|$ is referred to as the *fringe amplitude or visibility* while the argument $\phi_{\mathcal{V}}$ is the *fringe phase*. $A_N(\vec{\sigma})$ represents the normalized pattern that quantifies how off-axis signals are attenuated as they are received by a given antenna or telescope. In this treatment the astronomical object is assumed to be small in angular size in order to ignore the curvature of the celestial sphere.

The physical baseline \vec{B} can be decomposed into components $\vec{u} = (u, v)$ in units of observing wavelength along the east and north directions (respectively) as projected in the direction of our target. The vector $\vec{\sigma} = (l, m)$ also can be represented in rectilinear coordinates on the celestial sphere, where l points along local east and m points north². Here, l and m both have units of radians. Equation 1 now becomes:

$$\tilde{\mathcal{V}}(u, v) = |\mathcal{V}|e^{i\phi_{\mathcal{V}}} = \int_{l,m} A_N(l, m)I(l, m)e^{-2\pi i(ul+vm)}dldm \quad (2)$$

The fundamental insight from Equation 2 is that an interferometer is a Fourier Transform machine – it converts an intensity distribution $I(l, m)$ into measurements of Fourier components $\tilde{\mathcal{V}}(u, v)$ for all the baselines in the array represented by the (u, v) coverage. Since an intensity distribution can be described fully in either image space or Fourier space, the collection of sufficient Fourier components using interferometry allows for an image reconstruction through an inverse Fourier Transform process, although practical limitations lead to compromises in the quality of such images.

2.3. Interferometry in practice

In this section, the similarities and differences between radio and optical interferometers are summarized along with the reasons for the main differences. Interested readers can find more detailed on specific hardware implementations in Volume I of this series.

Modern radio and optical interferometers typically use conventional steerable telescopes to collect photons from the target. In the radio, a telescope is often called an antenna; it is typically

²There are several different coordinate systems in use to describe the geometry of ground-based interferometers used in observing the celestial sphere; (see e.g. Thompson et al. 2001, Chapter 4 and Appendix 4.1).

a parabolic reflector with a very short focal length ($f/D \approx 0.35$ is common), with signal collection and initial amplification electronics located at the prime focus. Owing to the large value of $\Delta\Theta \sim \frac{\lambda}{\text{Diameter}}$, the diffraction pattern of the antenna aperture is physically a relatively large region at the prime focus. This fact, coupled with the cost and complexity of duplicating and operating many low-noise receivers in close proximity to each other, has meant that antennas used in radio astronomy typically have only a “single-pixel” signal collection system (a dipole or a “feed horn”) at the prime focus³. Light arriving from various directions on the sky are attenuated depending on the shape of the diffraction pattern, written as A_N in Equation 2 and often called the “antenna pattern” or the “primary beam”. The signal collection system may be further limited to a single polarization mode, although systems are common that simultaneously accept both linear (or both circular) polarization states. After initial amplification, the signal is usually mixed with a local oscillator to “down-convert” the high frequencies to lower frequencies that can more easily be amplified and processed further. These lower-frequency signals from the separate telescopes can also be more easily transported over large distances to a common location using e.g. coaxial cable, or by modulating an optical laser and using fiber optics. This common location houses the “back end” of the receiver, where the final steps in signal analysis are carried out including band definition, correlation, digitizing, and spectral analysis. In some cases, the telescope signals are recorded onto magnetic media and correlated at a later time and in a distant location (e.g. the “Very Long Baseline Array” or global VLBI).

In the optical, the light from the object is generally focused by the telescope, re-collimated into a compressed beam for free-space transport, and then sent to a central location in a pipe which is typically evacuated to avoid introducing extra air dispersion and ground-level turbulence. In rare cases, the light at the telescope is focused directly into a single-mode fiber, which is the dielectric equivalent to the metallic waveguides used in radio and millimeter receivers. Note that atmospheric seeing is very problematic for even small visible and infrared telescopes while it is usually negligible compared to the diffraction limit for even the largest radio and mm-wave telescopes.

Both radio and optical interferometers must delay the signals from some telescopes to match the optical paths. After mixing to a lower frequency, radio interferometers can use switchable lengths of coaxial cable in order to introduce delays. More recently, the electric fields can be directly digitized with bandwidths of > 5 GHz, and these “bits” can be saved in physical memory and then recalled at a later time. For visible and infrared systems, switchable fiber optics are not practical due to losses and glass dispersion; the only solution is to use an optical “free-space” delay line consisting of a retroreflector moving on a long track and stabilized through laser metrology to compensate for air path disturbances and vibrations in the building.

In a radio interferometer, once all the appropriate delays have been introduced the signals from each telescope can be combined. Early radio signal correlators operated in an “optical” mode

³Very recently, several radio observatories have begun to equip their antennas (and at least one entire synthesis telescope) with arrays of such feeds.

as simple adding interferometers, running the sum of the signals from the two arms through a square-law detector. The output of such a detector contains the product of the two signals. Unfortunately, the desired correlation product also comes with a large total power component caused by temporally-uncorrelated noise photons contributed (primarily) by the front-end amplifiers in each arm of the interferometer plus atmosphere and ground noise. This large signal demanded excellent DC stability in the subsequent electronics, and it was not long in the history of radio interferometry before engineers found clever switching and signal-combination techniques to suppress the DC component. These days signal combiners deliver only the product of the signals from each arm, and are usually called “correlators”⁴. Most modern radio/millimeter arrays use digital correlators that introduce time lags between all pairs of telescopes in order to do a full temporal cross-correlation. This allows a detailed wavelength-dependent visibility to be measured, i.e., an interferometric spectrum with $R = \frac{\lambda}{\Delta\lambda} > 100000$ if necessary. By most metrics, radio correlators have reached their fundamental limit in terms of extracting full spectral and spatial information and can be fairly sophisticated and complex to configure when correlating multiple bandpasses simultaneously with high spectral resolution⁵.

In the visible and infrared, the electric fields can not be further amplified without strongly degrading the signal-to-noise ratio, and so parsimonious beam combining strategies are common that split the signal using e.g. partly-reflecting mirrors into a small number of pairs or triplets. Furthermore, most optical systems have only modest spectral resolutions of typically $R \sim 40$ in order to maintain high signal-to-noise ratio, although a few specialized instruments exist that reach $R > 1000$ or even $R > 30000$. Signal combination finally takes place simply by mixing the light beams together and modulating the relative optical path difference, either using spatial or temporal encoding. The total power measurement in a visible-light or infrared detector will reveal the interference fringe and a Fourier analysis can be used to extract the complex visibility $\tilde{\mathcal{V}}$.

Because the ways of measuring visibilities are quite different, radio and optical interferometrists typically report results in different units. Radio/mm interferometers measure correlated flux density in units of Jansky ($10^{-26} \text{ W m}^{-2} \text{ Hz}^{-1}$), just as suggested by Equation 2⁶. In the optical however, interferometers tend to always measure a normalized visibility that varies from 0 to 1 – this is simply the correlated signal normalized by the total power. One can convert the latter to correlated

⁴This is not all advantageous; if the data is intended to be used in an imaging synthesis, the absence of the total power component means that the value of the map made from the data will integrate to zero. In other words, without further processing the image will be sitting on a slightly-negative “floor”. If more interferometer spacings around zero are also missing, the floor becomes a “bowl”. All this is colloquially called “the short-spacing problem”, and it adversely affects the photometric accuracy of the image. A significant part of the computer processing “bag of tricks” used to “restore” such images is intended to address this problem, although the only proper way to do that is to obtain the missing data and incorporate it into the synthesis.

⁵At millimeter and sub-millimeter wavelengths, correlators still do not attain the maximum useful bandwidths for continuum observations

⁶Recall that an integration of specific intensity over solid angle results in a flux density, often expressed in Jansky.

flux density by simply multiplying by the known total flux density of the target at the observed wavelengths, or otherwise by carrying out a calibration of the system by a target of known flux density.

2.3.1. Quantum limits of amplifiers

The primary reason why radio and optical interferometers differ so much in their detection scheme is because coherent amplifiers would introduce too much extraneous noise at the high frequencies encountered in the optical and infrared. This difference is fundamental and is explored in more detail in this section.

At radio frequencies there are huge numbers of photons in a typical sample of the electromagnetic field, so the net phase of a packet of radio photons (either from the source or from a noisy receiver) is well-defined and amplifiers can operate coherently. The ultimate limits which apply to such amplifiers are dictated by the uncertainty principle as stated by Heisenberg. Beginning with the basic “position - uncertainty” relation $\Delta x \Delta p_x \geq h/4\pi$, it is easy to derive the “energy - time” relation $\Delta E \Delta t \geq h/4\pi$. Since the uncertainty in the energy of the n photons in a wave packet can be written as $\Delta E = h\nu \Delta n$ and the uncertainty in the phase of the aggregate as $\Delta\phi = 2\pi\nu \Delta t$, this leads to the equivalent uncertainty relation $\Delta\phi \Delta n \geq 1/2$.

An ideal amplifier which adds no noise to the input photon stream leads to a contradiction of the uncertainty principle. The following argument shows how this happens (adapted from Heffner 1962): Consider an ideal coherent amplifier of gain G which creates new photons in phase coherence with the input photons, and assume it adds no incoherent photons of its own to the output photon stream. With n_1 photons going into such an amplifier, there will be $n_2 = Gn_1$ photons at the output, all with the same phase uncertainty $\Delta\phi_2 = \Delta\phi_1$ with which they went in. In addition, in this model it is expected that $\Delta n_2 = G\Delta n_1$ (no additional “noise” photons unrelated to the signal). But according to the same uncertainty relation, the photon stream coming out of the amplifier must also satisfy $\Delta\phi_2 \Delta n_2 \geq 1/2$. This would imply that $\Delta\phi_1 \Delta n_1 \geq \frac{1}{2G}$, which for large G says that the input photon number and wave packet phase could be measured with essentially no noise. But this contradicts the same uncertainty relation for the input photon stream, which requires that $\Delta\phi_1 \Delta n_1 \geq 1/2$. This contradiction shows that one or more of our assumptions must be wrong. The argument can be saved if the amplifier itself is required to add noise of its own to the photon stream; the following heuristic construction shows how. Using the identity $\Delta n_2 = (G - N) \cdot \Delta n_1 + N\Delta n_1$ at the output (where N is an integer $N \geq 1$), and referring this noise power back to the input by dividing it with the amplifier gain G , this leads to $(1 - N/G) \cdot \Delta n_1 + (N/G) \cdot \Delta n_1$ at the input to the amplifier, which for large G is Δn_1 . The smallest possible value of N is 1. This preserves the uncertainty relation at the expense of an added minimum noise power of $h\nu$ at the input. Oliver (1965) has elaborated and generalized this argument to include all wavelength regimes, and has shown that the minimum total noise power spectral density ψ_ν of an ideal amplifier (relative to the

input) is

$$\psi_\nu = \frac{h\nu}{e^{(h\nu/kT)} - 1} + h\nu \text{ Watts/Hz} , \quad (3)$$

where T is the kinetic temperature that the amplifier input faces in the propagation mode to which the amplifier is sensitive. For $h\nu < kT$ this reduces to $\psi_\nu \approx kT$ Watts/Hz, which can be called the "thermal" regime of radio astronomy. For $h\nu > kT$ this becomes $\psi_\nu \approx h\nu$ Watts/Hz in the "quantum" regime of optical astronomy. The crossover point where the two contributions are equal is where $h\nu/kT = \ln 2$, or at $\lambda_c \cdot T_c = 20.75$ (mm K). As an illustration of the use of this equation, consider this example: The sensitivity of high-gain radio-frequency amplifiers can usually be improved by reducing their thermodynamic temperatures. However, for instance at a wavelength of 1 mm, it might be unnecessary (depending on details of the signal chain) to aim for a high-gain amplifier design to lower the thermodynamic temperature below about 20K, since at that point the sensitivity is in any case limited by quantum noise. At even shorter wavelengths, the rationale for cooled amplifiers disappears, and at optical wavelengths amplifiers are clearly not useful since the noise is totally dominated by spontaneous emission⁷ and is equivalent to thermal emission temperatures of thousands of degrees. The extremely faint signals common in modern optical observational astronomy translate into very low photon rates, and the addition of such irrelevant photons into the data stream by an amplifier would not be helpful.

2.4. Atmospheric Turbulence

So far, the analysis of interferometer performance has assumed a perfect atmosphere. However, the electromagnetic signals from cosmic sources are distorted as they pass through the intervening media on the way to the telescopes. These distortions occur first in the interstellar medium, followed by the interplanetary medium in the solar system, then the Earth's ionosphere, and finally the Earth's lower atmosphere (the troposphere) extending from an altitude of ≈ 11 km down to ground level. The media involved in the first three sources of distortion contain ionized gas and magnetic fields, and their effects on signal propagation depend strongly on wavelength (generally as $\propto \lambda^2$) and polarization. At wavelengths shorter than about 10 cm the troposphere begins to dominate. Molecules in the troposphere (especially water vapor) become increasingly troublesome at frequencies above 30 GHz (1 cm wavelength), and the atmosphere is essentially opaque beyond 300 GHz except for two rather narrow (and not very clear) "windows" from 650-700 and 800-900 GHz which are usable only at the highest-altitude sites. The next atmospheric windows appear in the IR at wavelengths less than about 15 microns. The optical window opens around one micron, and closes again for wavelengths shorter than about 350 nm.

The behavior of the troposphere is thus of prime importance to ground-based astronomy at

⁷Although amplifiers are currently used in the long-distance transmission of near-IR (digital) communication signals in optical fibers, the signal levels are relatively large and low noise is not an important requirement.

wavelengths from the decimeter-radio to the optical. Interferometers are used in the study of structure in the troposphere, and a summary of approaches and results with many additional references is given in Thompson et al. (2001); Carilli & Holdaway (1999); Sutton & Hueckstaedt (1996, Ch. 13). A discussion oriented towards optical wavelengths can be found in Quirrenbach (2000). Since the main focus here is on using interferometers to measure the properties of the cosmic sources themselves, our discussion is limited to some “rules of thumb” for choosing the interferometer baseline length and the time interval between measurements of the source and of a calibrator in order to minimize the deleterious effects of propagation on the fringe amplitudes and (especially) fringe phases.

2.4.1. Phase fluctuations – length scale

Owing to random changes in the refractive index of the atmosphere and the size distribution of these inhomogeneities, the path length for photons will be different along different parallel lines of sight. This fluctuating path length difference grows almost linearly with the separation d of the two lines of sight for separations up to some maximum, called the outer scale length (typically tens to hundreds of meters, with some weak wavelength dependence), and is roughly constant beyond that. Surprisingly, in spite of the differences in the underlying physical processes causing refraction, variations in the index of refraction are quite smooth across the visible and all the way through to the radio. At short radio wavelengths, the fluctuations are dominated by turbulence in the water vapor content; at optical/IR wavelengths, it is temperature and density fluctuations in dry air that dominate.

Using a model of fully-developed isotropic Kolmogorov turbulence for the Earth’s atmosphere, the rms path length difference grows according to $\sigma_d \propto d^{5/6}$ for a path separation d (see Thompson et al. 2001, Ch. 13, for references). High altitude sites show smaller path length differences as the remaining vertical thickness of the water vapor layer decreases. Relatively large seasonal and diurnal variations also exist at high mountain sites as the atmospheric temperature inversion layer generally rises during the summer and further peaks during mid-day. Variations in σ_d by factors of ~ 10 are not unusual (see Thompson et al. 2001, Fig. 13.13), but a rough average value for a good observing site is $\sigma_d \approx 1$ mm for baselines $d \approx 1$ km at millimeter wavelengths, and $\sigma_d \approx 1$ micron for baselines $d \approx 50$ cm at infrared wavelengths.

The length scale fluctuations translate into fringe phase fluctuations of $\sigma_\phi = 2\pi\sigma_d/\lambda$ in radians. The *maximum coherent baseline* d_0 is defined as that baseline length for which the rms phase fluctuations reach 1 radian. Using the expressions in the previous paragraph and coefficients suitable for the radio and optical ranges at the better observing sites, two useful approximations are $d_0 \approx 140 \cdot \lambda^{6/5}$ meters for λ in millimeters (useful at millimeter radio wavelengths), and $d_0 \approx 10 \cdot \lambda^{6/5}$ centimeters for λ in microns (useful at IR wavelengths). These two expressions are in fact quite similar; using the “millimeter expression” to calculate d_0 in the IR underestimates the value obtained from the “IR expression” by a factor of 2.8, which is at the level of precision to be expected.

At shorter wavelengths (visible and near-infrared), atmospheric turbulence limits even the image quality of small telescopes. This has led to a slightly different perspective for the length scale that characterizes atmospheric turbulence, although it is closely related to the previous description. The Fried length r_0 (Fried 1965) is the equivalent-sized telescope diameter whose diffraction limit matches the image quality through the atmosphere due to *seeing*. It turns out that this quantity is proportional to the length scale where the rms phase error over the telescope aperture is ≈ 1 radian. In other words, apertures with diameters small compared to r_0 are approximately diffraction limited, while larger apertures have resolution limited by turbulence to $\approx \lambda/r_0$. It can be shown that, for an atmosphere with fully-developed Kolmogorov turbulence, $r_0 \approx 3.2d_0$ (Thompson et al. 2001, Ch. 13).

2.4.2. Phase fluctuations – time scale

Although fluctuations of order one radian may be no more than a nuisance at centimeter wavelengths, requiring occasional phase calibration (see §3.1.3), they will be devastating at IR and visible wavelengths owing to their rapid variations in time. In order to relate the temporal behavior of the turbulence to its spatial structure, a model of the latter is required along with some assumption for how that structure moves over the surface of the Earth. One specific set of assumptions is described in Thompson et al. (2001, Ch. 13); however, for the purposes here it is sufficient to use Taylor’s “frozen atmosphere” model with a nominally-static phase screen that moves across the Earth’s surface with the wind at speed v_s . This phase screen traverses the interferometer baseline d in a time $\tau_d = d/v_s$, at the conclusion of which the total path length variation is σ_d . Taking the critical time scale τ_c to be when the rms phase error reaches 1 radian, then $\tau_c \approx d_0/v_s$ with d_0 given in the previous paragraph. As an example consider a wind speed of 10 m/s; this leads to $\tau_c \approx 14$ seconds at $\lambda = 1$ mm, and ≈ 10 milliseconds at $\lambda = 1$ micron. Clearly the techniques required to manage these variations will be very different at the two different wavelength regimes, even though the magnitude of the path length fluctuations (in radians of phase) are similar. Representative values of these quantities are collected in Table 2.

2.4.3. Calibration – Isoplanatic Angle

The routine calibration of interferometer phase and amplitude is usually done by observing a source with known position and intensity inter-leaved in time with the target of interest. At centimeter wavelengths and longer, the discussion in the previous section indicates that such measurements can be done on time scales of minutes to hours, providing ample time to re-position telescopes elsewhere on the sky in order to observe a calibrator. But how close to the target of interest does such a calibrator have to be? Ideally, the calibrator ought to be sufficiently nearby on the celestial sphere that the line of sight traverses a part of the atmosphere with substantially the same phase delay as the line of sight to the target. This angle is called the *isoplanatic angle* Θ_{iso} ;

it characterizes the angular scale size over which different parts of the incoming wavefront from the target encounter closely similar phase shifts, thereby minimizing the image distortion. The isoplanatic angle can be roughly estimated by calculating the angle subtended by an r_0 -sized patch at a height h that is characteristic for the main source of turbulence; hence, roughly $\Theta_{iso} \approx \frac{r_0}{h}$. Within a patch on the sky with this angle, the telescope/interferometer PSF remains substantially constant, retaining the convolution relation between the source brightness distribution and the image. Some approximate values are given in Table 2 as a guide.

At visible and near-IR wavelengths, Table 2 shows that the isoplanatic angle is very small, smaller than an arcminute. Unfortunately, the chance of having a suitably bright and point-like object within this small patch of the sky is very low. Even if an object did exist, it would be nearly impossible to repetitively re-position the telescope and delay line at the milli-second level timescale needed to “freeze” the turbulence between target and calibrator measurements. Special techniques to deal with this problem will be discussed further in section 3.1.3.

3. Planning Interferometer Observations

The issues to consider when writing an interferometer observing proposal or planning the observations themselves include: the desired sensitivity (i.e., the unit telescope collecting area, the number of telescopes to combine at once, the amount of observing time), the required field-of-view and angular resolution (i.e., the shortest and longest baselines), calibration strategy and expected systematic errors (i.e., choosing phase and amplitude calibrators), the expected complexity in the image (i.e., the completeness of u,v coverage, do science goals demand model-fitting or model-independent imaging), and the spectral resolution (i.e., correlator settings, choice of combiner instrument). Many of these issues are intertwined, and the burden on the aspiring observer to reach a compatible set of parameters can be considerable. Prospective observers planning to use the VLA are fortunate to have a wide variety of software planning tools and user’s guides already at their disposal, but those hoping to use more experimental facilities or equipment which is still in the early phases of commissioning will find their task more challenging.

Here, the most common issues encountered during interferometer observations will be introduced. In many ways this is more of a list of things to worry about rather than a compendium of solutions. The basic equations and considerations have been collected in Table 3. In order to obtain the latest advice on optimizing a request for observing time, or to plan an observing run, observers ought to consult the web sites, software tools, and human assistants available for them at each installation (see Appendix for a list of current facilities).

Table 2. Approximate baseline length, Fried length, and time scales for a 1-radian rms phase fluctuation in the Earth’s troposphere and a wind speed of 10 m/s.^a

Wavelength	Max. Coherent Baseline d_0	Fried length r_0	Time scale τ_c	Isoplanatic angle at zenith Θ_{iso}
0.5 μm (visible)	4.4 cm	14 cm	4.4 ms	5.5''
2.2 μm (near-IR)	26 cm	83 cm	26 ms	33''
1 mm (millimeter)	140 m	450 m	14 sec	3.5°
10 cm (radio)	35 km	112 km	58 min	large ^b

^a From parameters for Kolmogorov turbulence given in Thompson et al. (2001, Ch. 13), and in Woolf (1982, Table 2). The inner and outer scale lengths are presumed to remain constant in these rough approximations. Values are appropriate for a good observing site and improve at higher altitudes. See §2.4 for more discussion.

^b Limited in practice by observing constraints such as telescope slew rates and elevation limits, and source availability.

Table 3. Planning Interferometer Observations

Consideration	Equation
Angular Resolution	$\Theta = \frac{1}{2} \frac{\lambda}{B_{\text{max}}}$
Spectral Resolution	$R = \frac{\lambda}{\Delta\lambda} = \frac{c}{\Delta\nu}$
Field-of-View	
<i>primary beam</i>	$\Delta\Theta \sim \frac{\lambda}{D_{\text{Telescope}}}$
<i>bandwidth-smearing</i>	$\Delta\Theta \sim R \cdot \frac{\lambda}{B_{\text{max}}}$
<i>time-smearing</i>	$\Delta\Theta \sim \frac{B_{\text{max}}}{230} \frac{\lambda}{\Delta t_{\text{minutes}}}$
Phase Referencing	
<i>Coherence Time</i>	see Table 2
<i>Isoplanatic Angle</i>	see Table 2

3.1. Sensitivity

Fortunately modern astronomers can find detailed documentation on the expected sensitivities for most radio and optical interferometers currently available. Indeed, the flexibility of modern instrumentation sometimes defies a back-of-the-envelope estimation for the true signal-to-noise ratio (SNR) expected for a given observation. In order to better understand what limits sensitivity for real systems, the dominant noise sources and the key parameters affecting signal strength are introduced. Most of the focus will be for observations of point sources since resolved sources do not contribute signal to all baselines in an array and this case must be treated with some care.

Here, the discussions of the radio and optical cases are separate because of the large differences in the nature of the noise processes (e.g., see §2.3.1) and the associated nomenclature. Radio and optical observations lie at the two limits of Bose-Einstein quantum statistics that govern photon arrival rates (e.g., Pathria 1972, see §6.3). At long wavelengths, the occupation numbers are so high that the statistics evolve into the Gaussian limit and where the root-mean-square (rms) fluctuation in the detected power ΔP is proportional to the total power P itself (e.g., $\Delta \text{Power} \propto \text{Power}$). On the other hand, in the optical limit, the sparse occupation of photon states results in the familiar Poisson statistics where the level of photon fluctuations ΔN is proportional to \sqrt{N} . Most of the SNR considerations for interferometers are in common with single-dish radio and standard optical photometry, and so interested readers are referred to the relevant chapters in Volumes 1 and 2 of this series.

3.1.1. Radio Sensitivity

The signal power spectral density P_ν received by a radio telescope of effective area A_e (m^2) from a celestial point source of flux density S_ν (Jansky = Watts/ m^2 /Hz) is $P_\nu = A_e \cdot S_\nu$ (Watts/Hz). It is common to express this as the power which would be delivered to a radio circuit (wire, coaxial cable, or waveguide) by a matched termination at a physical temperature T_A , called the “antenna temperature”, so that $T_A = A_e S_\nu / 2k$ (Kelvin) where k = Boltzmann’s constant and the factor 1/2 accounts for the fact that, although the telescope’s reflecting surface concentrates both states of polarization at a focus, the “feed” collects the polarization states separately. As described in section 2.3.1, the amplifier which follows must add noise; this additional noise power (along with small contributions from other extraneous sources in the telescope field of view) P_ν^s can likewise be expressed as $P_\nu^s = kT_s/2$, where T_s is the “system temperature.” The rms fluctuations in this noise power will limit the faintest signals that can be distinguished. As mentioned in the previous paragraph, these fluctuations are directly proportional to the receiver noise power itself, so $\Delta T_s \propto T_s$. They will also be inversely proportional to the square root of the number of samples of this noise present in the receiver passband. The coherence time of a signal in a bandwidth $\Delta\nu$ is proportional to $1/\Delta\nu$, so in an integration time τ there are of order $\tau\Delta\nu$ independent samples of the noise, and the statistical uncertainty will improve as $1/\sqrt{\tau\Delta\nu}$. The ratio of the rms receiver

noise power fluctuations to the signal power is therefore:

$$\Delta T_s/T_A \propto \frac{2kT_s}{A_e S \sqrt{\tau \Delta\nu}} . \quad (4)$$

The minimum detectable signal ΔS is defined as the value of S for which this ratio is unity. For this “minimum” value of S the equation becomes:

$$\Delta S = \frac{f_c \cdot kT_s}{A_e \sqrt{\tau \Delta\nu}} , \quad (5)$$

The coefficient of proportionality f_c for this equation is of order unity, but the precise value depends on a number of details of how the receiver operates. These details include whether the receiver output contains both polarization states, whether both the in-phase and the quadrature channels of the complex fringe visibility are included, whether the receiver operates in single- or double-sideband mode, and how precisely the noise is quantized if a digital correlator is used. Further discussion of the various possibilities is given in Thompson et al. (2001, Chapter 6). For the present purpose, it suffices to notice that the sensitivity for a specific radio interferometer system improves only slowly with integration time and with further smoothing of the frequency (radial velocity) resolution. The most effective improvements are made by lowering the system temperature and by increasing the collecting area.

The point-source sensitivity continues to improve as telescopes are added to an array. An array of n identical telescopes contains $N_b = n(n-1)/2$ distinct baselines. If the signals from each telescope are split into multiple copies, N_b interference pairs can be made. The rms noise in the flux density on a point source including all the data is then

$$\Delta S = \frac{f_c \cdot kT_s}{A_e \sqrt{N_b \tau \Delta\nu}} . \quad (6)$$

So far the discussion has been made for isolated point sources. Extended sources are physically characterized by their surface brightness power spectral density $B_{\text{surf}}(\alpha, \delta, \nu)$ (Jansky/steradian) and by the angular resolution of the observation as expressed by the solid angle Ω_b of the synthesized beam in steradians (see §5). By analogy with the discussion of rms noise power from thermal sources given earlier, it is usual to express the surface brightness power spectral density for an extended sources in terms of a temperature. This conversion of units to Kelvins is done using the Rayleigh-Jeans approximation to the Planck black-body radiation law, although the radiation observed in the image is only rarely thermally-generated. The conversion from $B_{\text{surf}}(\alpha, \delta, \nu)$ (Jansky/steradian) to T_b in Kelvins is

$$T_b = \frac{\lambda^2 B_{\text{surf}}}{2k\Omega_b} , \quad (7)$$

which requires ($h\nu/kT \ll 1$) if the radiation is thermal; otherwise, this conversion can be viewed merely as a convenient change of units. The rms brightness temperature sensitivity in a radio synthesis image from receiver noise alone is then

$$\Delta T_b = \frac{f_c \lambda^2 T_s}{2A_e \Omega_b \sqrt{N_b \tau \Delta\nu}} . \quad (8)$$

The final equations above for the sensitivity on synthesis imaging maps shows that the more elements one has, the better the flux density sensitivity will be. For example if one compares an array of $N_b = 20$ baselines with an array containing $N_b = 10$ baselines, the flux density SNR is improved by a factor $\sqrt{2}$ no matter where the additional 10 baselines are located in the u, v plane. However, the brightness temperature sensitivity does depend critically on the actual distribution of baselines used in the synthesis. For instance, if the same number of telescopes is “stretched out” to double the maximum extent on the ground, the equations above show that the flux density sensitivity ΔS remains the same, but the brightness temperature sensitivity ΔT_b is worse by a factor of 4 since the synthesized beam is now 4 times smaller in solid angle. This is a serious limitation for spectral line observations where the source of interest is (at least partially) resolved and where the maximum surface brightness is modest. For instance, clouds of atomic hydrogen in the Galactic ISM never seem to exceed surface brightness temperatures of ≈ 80 K, so the maximum achievable angular resolution (and hence the maximum useable baseline in the array) is limited by the receiver sensitivity. This can only be improved by lowering the system temperature on each telescope or by increasing the number of interferometer measurements with more telescopes and/or more observing time.

A cautionary note is appropriate here. In the case of an optical image of an extended object taken e.g. with charge-coupled device (CCD) camera on a filled aperture telescope, a simple way of improving the SNR is to average neighboring pixels together thereby creating a smoothed image of higher brightness sensitivity. At first sight, the equation for ΔT_b above suggests that this should also happen with synthesis images, but here the improvement is not as dramatic as it may seem at first sight. The reason is that the action of smoothing is equivalent to discarding the longer baselines in the u, v plane; for instance, reducing the longest baseline used in the synthesis by a factor of 2 would indeed lead to an image with brightness temperature sensitivity which is better by a factor of 2^2 , but the effective reduction of the number of interferometers from N to $N/2$ means that the net improvement is only $2^{1.5}$. A better plan would have been to retain all the interferometers but to shrink the array diameter with the factor 2 by moving the telescopes into a more compact configuration. This is one reason why interferometer arrays are usually constructed to be reconfigurable.

3.1.2. *Visible and Infrared Sensitivity*

As mentioned earlier, the visible and infrared cases deviate substantially from the radio case. While the sensitivity is still dependent on the collecting area of the telescopes (A_e), the dominant noise processes behave quite differently. In the visible and infrared (V/IR), noise is generated by the random arrival times of the photons governed by Poisson statistics $\Delta N = \sqrt{N}$, where N is the mean number of photons expected in a time interval τ and ΔN is the rms variation in the actual measured number of photons. Depending on the observing setup (e.g., the observing wavelength, spectral resolution, high visibility case or low visibility case), the dominant noise term

can be Poisson noise from the source itself, Poisson noise from possible background radiation, or even detector noise. Because of the centrality of Poisson statistic, it is common to work in units of total detected photo-electrons N within a time interval τ , rather than power spectral density P_ν or system temperature T_S . This conversion is straightforward:

$$N = \eta \frac{P_\nu \Delta\nu}{h\nu} \tau \tag{9}$$

$$= \eta \frac{S_\nu A_e \Delta\nu}{h\nu} \tau \tag{10}$$

where η represents the total system detection efficiency which is the combination of optical transmission of system and the quantum efficiency of the detector and the other variables are the same as for the radio case introduced in the last section.

For the optical interferometer, atmospheric turbulence limits the size of the aperture that can be used without adaptive optics (the atmosphere does not limit the useful size of the current generation of single-dish mm-wave and radio telescopes). The Fried parameter r_0 sets the coherence length and thus the $\max(A_e) \sim r_0^2$. Likewise without corrective measures, the longest useful integration time is limited to the atmospheric coherence time $\tau \sim \tau_c$. There exists a *coherent volume* of photons that can be used for interferometry, scaling like $r_0 \cdot r_0 \cdot c\tau_c$. As an example, consider the coherent volume of photons for decent seeing conditions in the visible ($r_0 \sim 10$ cm, $\tau_c \sim 3.3$ ms). From this, the limiting magnitude can be estimated by requiring at least 10 photons to be in this coherent volume. Assuming a bandwidth of 100 nm, 10 photons ($\lambda \sim 550$ nm) in the above coherent volume corresponds to a V magnitude of 11.3, which is the best limit one could hope to achieve⁸. This is more than 14 magnitudes worse than faint sources observed by today’s 8-m class telescopes that can benefit from integration times measured in hours instead of milli-seconds. Because the atmospheric coherence lengths and timescales behave approximately like $\lambda^{\frac{6}{5}}$ for Kolmogorov turbulence, the coherent volume $\propto \lambda^{\frac{18}{5}}$. Until the deleterious atmospheric effects can be neutralized, ground-based optical interferometers will never compete with even small single-dish telescopes in raw point-source sensitivity.

Under the best case the only source of noise is Poisson noise from the object itself. Indeed, this limit is nearly achieved with the best visible-light detectors today that have read-noise of only a few electrons. More commonly, especially in the infrared, detectors introduce the noise that limits sensitivity, typically 10-15 electrons of read-noise in the near-IR for the short exposures required to effectively freeze the atmospheric turbulence. For wavelengths longer than about $2.0\mu\text{m}$ (i.e., K, L, M, N bands), Poisson noise from the thermal background begins to dominate over other sources of noise. Highly-sensitive infrared interferometry will require a space platform that will allow long coherence times and low thermal background. Please consult the observer manual for each specific

⁸Real interferometers will have a realistic limit about 1-2 orders of magnitude below the theoretical limit due to throughput losses and non-ideal effects such as loss of system visibility.

interferometer instrumentation to determine point-source sensitivity.

Another important issue to consider is that a low visibility fringe ($\mathcal{V} \ll 1$) is harder to detect than a strong one. Usually fringe detection sets the limiting magnitude of an interferometer/instrument, and this limit often scales like $N\mathcal{V}$, the number of “coherent” photons. For readnoise or background noise dominant situations (common in NIR), this means that if the point-source ($\mathcal{V} = 1$) limiting magnitude is 7.5 then a source with $\mathcal{V} = 0.1$ would need to be as bright as magnitude 5.0 to be detected. The magnitude limit worsens even more quickly for low visibility fringes when noise from the source itself dominates, since brighter targets bring along greater noise. Another common expression found in the literature is that the SNR for a visible-light interferometer scales like $N\mathcal{V}^2$. This latter result can be derived by assuming that the “signal” is the average power spectrum $(N\mathcal{V})^2$ and the dominant noise process is photon noise which has a power spectrum that scales like N here.

3.1.3. *Overcoming the Effects of the Atmosphere: Phase Referencing, Adaptive Optics, and Fringe Tracking*

As discussed above, the limiting magnitude will strongly depend on the maximum coherent integration time that is set by the atmosphere. Indeed, this limitation is very dramatic, restricting visible-light integrations to mere milli-seconds and millimeter radio observations to a few dozen minutes. For mm-wave and radio observations, the large isoplanatic angle and long atmospheric coherence times allow for real-time correction of atmospheric turbulence by using *phase referencing*.

In a phase-referencing observing sequence, the telescopes in the array will alternate between the (faint) science target and a (bright) phase calibrator nearby in the sky. If close enough in angle (within the isoplanatic patch), then the turbulence will be the same between the target and bright calibrator; thus, the high SNR measurement of fringe phase on the calibrator can be used to account for the atmospheric phase changes. Another key aspect is that the switching has to be fast enough that the atmospheric turbulence does not change between the two pointings. With today’s highly-sensitive radio and mm-wave receivers, enough bright targets exist to allow nearly full sky coverage so that most faint radio source will have a suitable phase calibrator nearby.⁹ In essence, phase referencing means that a fringe does not need to be detected within a single coherence time τ_c but rather one can coherently integrate for as long as necessary with sensitivity improving as $1/\sqrt{t}$. In §4 a simple example is presented that demonstrates how phase-referencing works with simulated data.

In the visible and infrared, phase referencing by alternate target/calibrator sequences is practically impossible since $\tau_c \ll 1$ second and $\Theta_{\text{iso}} \ll 1$ arcminute isoplanatic patch size. In V/IR

⁹At the shortest sub-mm wavelengths, phase-referencing is quite difficult due to strong water vapor turbulence, but can be partially corrected using “water-vapor monitoring” techniques (e.g., Wiedner et al. 2001).

interferometry, observations still alternate between a target and calibrator in order to calibrate the statistics of the atmospheric turbulence but not for phase referencing. A special case exists for dual-star narrow-angle astrometry (Shao & Colavita 1992) where a “Dual Star” module located at each telescope can send light from two nearby stars down two different beam trains to be interfered simultaneously. At K band, the stars can be as far as $\sim 30''$ apart for true phase referencing. This approach is being attempted at the VLT (PRIMA, Delplancke et al. 2006) and Keck Interferometers (ASTRA, Woillez et al. 2010). This technique can be applied to only a small fraction of objects owing to the low sky density of bright phase reference calibrators.

Adaptive optics (AO) can be used on large visible and infrared telescopes to effectively increase the collecting area A_e term in our signal equation, allowing the full telescope aperture to be used for interferometry. AO on a 10-m class telescope potentially boosts infrared sensitivity by $\times 100$ over the seeing limit; however, this method still requires a bright enough AO natural or laser guide star to operate. Currently, only the VLT and Keck Interferometers have adaptive optics implemented for regular use with interferometry. A related technique of *fringe tracking* is in more widespread use, whereby the interferometer light is split into two channels so that light from one channel is used exclusively for measuring the changing atmospheric turbulence and driving active realtime path length compensation. In the meantime, the other channel is used for longer science integrations (at VLTI, Keck, CHARA). This method improves the limiting magnitude of the system at some wavelengths if the object is substantially brighter at the fringe tracking wavelength, such as for dusty reddened stars. Fringe tracking sometimes can be used for very high spectral observations of stars ordinarily too faint to observe at high dispersion.

It is important to mention these other optical interferometer subsystems (e.g., AO, fringe tracker) here because they are crucial for improving sensitivity, but the additional complexities do pose a challenge for observers. Each subsystem has its own sensitivity limit and now multiple wavelengths bands are needed to drive the crucial subsystems. As an extreme example, consider the Keck Interferometer Nuller (Colavita et al. 2009). The R-band light is used for tip-tilt and adaptive optics, the H band is used to correct for turbulence in air-filled Coude path, the K band is used to fringe track and finally the $10\mu\text{m}$ light is used for the nulling work. If the object of interest fails to meet the sensitivity limit of any of these subsystems then observations are not possible – most strongly affecting highly reddened sources like young stellar objects and evolved stars.

3.2. (u,v) Coverage

One central difference between interferometer and conventional single-telescope observations is the concept of (u,v) coverage. Instead of making a direct “image” of the sky at the focal plane of a camera, the individual fringe visibilities for each pair of telescopes are obtained. As discussed in §2.2, each measured complex visibility is a single Fourier component of a portion of the sky. The goal of this subsection is to understand how to estimate (u,v) coverage from the array geometry and which characteristics of Fourier coverage affect the final reconstructed image.

For a given layout of telescopes in an interferometer array, the Fourier coefficients can be measured and determined by drawing baselines between each telescope pair. To do this, an (x,y) coordinate system is first constructed to describe the positions of each element of the array; for ground-based arrays in the northern hemisphere, the convention is to orient the $+x$ axis towards the east and the $+y$ axis towards north. The process of determining the complete ensemble of (u,v) points provided by any given array can be laborious for arrays with a large number of elements. A simple method of automating the procedure is as follows. First, construct a distribution in the (x,y) plane of delta functions of unit strength at the positions of all elements. The (u,v) plane coverage can be obtained from the two-dimensional autocorrelation of this distribution, as illustrated in Figure 4 for four simple layouts of array elements. The delta functions for each array element are shown as dots in the upper row of sketches in this figure, and the corresponding dots in the u,v distributions are shown in the lower row of autocorrelations. Note that each point in the (u,v) plane is repeated on the other side of the origin owing to symmetry; of course the values of amplitude and phase measured on a source at one baseline will be the same whether one thinks of the baseline as extending from telescope 1 to telescope 2, or the converse. For an array of N telescopes, one can measure $\binom{N}{2} = \frac{(N)(N-1)}{2}$ independent Fourier components.

Sometimes the array geometry may result in the (near-)duplication of baselines in the (u,v) plane. This is the case for array #2 in the Figure 4, where the shortest spacing is duplicated 4 times, the next spacing is duplicated 3 times, the following spacing is duplicated twice, and only the longest spacing of this array is unique. While each of these interferometers does contribute statistically independent data as far as the noise is concerned, it is an inefficient use of hardware since the astrophysical information obtained from such redundant baselines is essentially the same. In order to optimize the Fourier coverage for a limited number of telescopes, a layout geometry should be *non-redundant*, with no baseline appearing more than once, so that the maximum number of Fourier components can be measured for a given array of telescopes. A number of papers have been written on how to optimize the range and uniformity of (u,v) coverage under different assumptions (Golay 1971; Keto 1997; Holdaway & Helfer 1999). Note that in the sketches of Figure 4, array #4 provides superior coverage in the u,v plane compared to arrays #3 and #2 with the same number of array elements.

Finally note that the actual (u,v) coverage depends not on the *physical baseline separations* of the telescopes but on the *projected baseline separations* in the direction of the target. For ground-based observing, a celestial object moves across the sky along a line of constant declination, so the (u,v) -coverage is actually constantly changing with time. This is largely a benefit since earth rotation dramatically increases the (u,v) -coverage without requiring additional telescopes. This type of synthesis imaging is often called *Earth rotation aperture synthesis*. The details depend on the observatory latitude and the target declination, and a few simple cases are presented in Figure 5. In general, sources with declinations very different from the local latitude will never reach a high elevation in the sky, such that the north-south (u,v) coverage will be foreshortened and the angular resolution in that direction correspondingly reduced.

Figure 6 shows the actual Fourier coverage for the 27-telescope Very Large Array (VLA) and for the 6-telescope CHARA Array. For $N = 27$, the VLA can measure 351 Fourier components while CHARA ($N = 6$) can measure only 15 simultaneously. Notice also in this figure that the ratio between the maximum baseline and the minimum baseline is much larger for the VLA (factor of 50, A array) compared to CHARA (factor of 10).

The properties of the (u,v)-coverage can be translated into some rough characteristics of the final reconstructed image. The final image will have an angular resolution of $\sim \frac{\lambda}{B_{\max}}$, and note that the angular resolution may not be the same in all directions. It is crucial to match the desired angular resolution with the maximum baseline of the array because longer baselines will over-resolve your target and have very poor (or non-existent) signal-to-noise ratio (see discussion §3.1.1). This functionally reduces the array to a much smaller number of telescopes which dramatically lowers both overall signal-to-noise ratio and the ability to image complex structures. For optical arrays that combine only 3 or 4 telescopes, relatively few (u,v) components are measured concurrently and this limits how much complicated structure can be reconstructed¹⁰. From basic information theory under best case conditions, one needs at least as many independent visibility measurements as the number of independent pixels in the final image. For instance, it will take hundreds of components to image a star covered with dozens of spots of various sizes, while only a few data points can be used to measure a binary system with unresolved components.

3.3. Field-of-view

While the (u,v) coverage determines the angular resolution and quality of image fidelity, the overall imaging field-of-view is constrained by a number of other factors.

A common limitation for field-of-view is the primary beam pattern of each individual telescope in the array and this was already discussed in §2.3: $\Delta\Theta \sim \frac{\lambda}{\text{Diameter}}$. This limit can be addressed by *mosaicing*, which entails repeated observations over a wide sky area by coordinating multiple telescope pointings within the array and stitching the overlapping regions together into a single wide-field image. This practice is most common in the mm-wave where the shorter wavelengths result in a relatively small primary beam. A useful rule of thumb is that your field-of-view (in units of the fringe spacing) is limited to the ratio of the baseline to the telescope diameter. Most radio and mm-wave imaging is limited by their primary beam, however there is a major push to begin using “array feeds” to allow imaging in multiple primary beams simultaneously.

Another limitation to field-of-view is the spectral resolution of the correlator/combiner. The spectral resolution of each channel can be defined as $R = \frac{\lambda}{\Delta\lambda}$. A combiner or correlator can not detect a fringe that is outside the system coherence envelope, which is simply related to the

¹⁰Fortunately, targets of optical interferometers are generally spatially compact and so sparser (u,v) coverage can often be acceptable.

spectral resolution R . The maximum observable field of view is R times the finest fringe spacing, or $\Delta\Theta \sim R \cdot \frac{\lambda}{B_{\max}}$, often referred to as the *bandwidth-smearing* limit. Most optical interferometers and also Very Long Baseline Interferometry (VLBI) are limited by bandwidth smearing.

A last limitation to field-of-view arises from temporal smearing of data by integrating for too long during an observation. Because the (u,v) coverage is constantly changing due to Earth rotation, time averaging removes information in the (u,v) -plane resulting in reduced field-of-view. A crude field-of-view limit based on this effect is $\Delta\Theta \sim \frac{230}{\Delta t_{\text{minutes}}} \frac{\lambda}{B_{\max}}$. Both radio and V/IR interferometric data can be limited by temporal-smearing if care is not taken in setting up the data collection, although this limitation is generally avoidable.

3.4. Spectroscopic Capabilities

As for regular radio and optical astronomy, one tries to observe at the crudest spectral resolution that is suitable for the science goal in order to achieve maximum signal-to-noise ratio. However as just discussed, spectral resolution does impact the imaging field-of-view, bringing in another dimension to preparations. While each instrument has unique capabilities that can not be easily generalized, most techniques will require dedicated spectral calibrations as part of observing procedures.

“Spectro-interferometry” is an exciting tool in radio and (increasingly) optical interferometry. In this application, the complex visibilities are measured in many spectral channels simultaneously, often across a spectrally-resolved spectral line. This allows the different velocity components to be imaged or modelled independently. For example, this technique can be used for observing emitting molecules in a young stellar object to probe and quantify Keplerian motion around the central mass or for mapping differential rotation on the surface of a rotating star using photospheric absorption lines (e.g., Kraus et al. 2008). Spectro-interferometry is analogous to “integral field spectroscopy” on single aperture telescopes, where each pixel in the image has a corresponding measured spectrum. Another clever example of spectro-interferometry pertains to maser sources in the radio: a single strong maser in one spectral channel can be used as a phase calibrator for the rest of the spectral channels (e.g., Greenhill et al. 1998).

4. Data Analysis Methods

After observations have been completed, the data must be analyzed. Every instrument will have a customized software pipeline to take the recorded electrical signals and transform into useful astronomical quantities. That said, the data reduction process is the similar for most systems and here the basic steps are outlined.

4.1. Data reduction and calibration overview

The goal of the data reduction is to produce calibrated complex visibilities and related observables such as closure phases (see §5.2.1). As discussed in §3, the basic paradigm for interferometric observing is to switch between data of well-known system calibrators and the target of interest. This allows for calibration of changing atmospheric conditions by monitoring the actual phase delay through the atmosphere (in radio) or by statistically correcting for decoherence from turbulence (in optical).

One begins by plotting the observed fringe amplitude versus time. Figure 7 shows a schematic example of how data reduction might proceed for the case of high quality radio interferometry observations, such as taken with the EVLA. Here the observed fringe amplitude and phase for a calibrator-target-calibrator sequence is presented. Notice that in this example the fringe amplitude of the calibrator is drifting up with time, as is the observed phase. As long as the switching time between target and calibrator is faster than instrumental gain drifts and atmospheric piston shifts, a simple function can be fitted to the raw calibrator measurements and then interpolated to produce the calibration curves to for the target. Here a 2nd order polynomial has been used to approximate the changing amplitude and phase response. This figure contains an example for only a single baseline, polarization, and spectral channel; there will be hundreds or thousands of panels like this in a dataset taken with an instrument as the EVLA or ALMA.

The justification for this fitting procedure can be expressed mathematically. As the wave traverses the atmosphere, telescope, and interferometer beamtrain/waveguides, the electric field can have its phase and amplitude modified.¹¹ These effects can be grouped together into a net complex *gain* of the system for each beam, $\tilde{\mathcal{G}}_i$ – the amplitude of $\tilde{\mathcal{G}}_i$ encodes the net amplification or attenuation of the field strength and the phase term corresponds to combination of time delays in the system and effects from amplifiers in the signal chain. Thus, the measured electric field \tilde{E}' can be written as a product of the original field \tilde{E} times this complex gain:

$$\tilde{E}' = \tilde{\mathcal{G}}\tilde{E} \tag{11}$$

Since the observed complex visibility $\tilde{\mathcal{V}}_{12}$ for a baseline between telescope 1 to telescope 2 is related to the product $\tilde{E}_1\tilde{E}_2^*$, then

$$\tilde{\mathcal{V}}'_{12} \propto \tilde{E}'_1\tilde{E}'_2{}^* \tag{12}$$

$$\propto \tilde{\mathcal{G}}_1\tilde{E}_1 \cdot \tilde{\mathcal{G}}_2^*\tilde{E}_2^* \tag{13}$$

$$\propto \tilde{\mathcal{G}}_1\tilde{\mathcal{G}}_2^*\tilde{\mathcal{V}}_{12} \tag{14}$$

Thus the measured complex visibility $\tilde{\mathcal{V}}'_{12}$ is closely related to the true $\tilde{\mathcal{V}}_{12}$, differing only by complex factor $\tilde{\mathcal{G}}_1\tilde{\mathcal{G}}_2^*$. By observing a calibrator with known structure, this gain factor can be measured,

¹¹In general, also the polarization states and wavefront coherence can also be modified.

even if the calibrator is not a point source for the interferometer. For a radio array, the gain factors are mainly associated with the individual telescope collectors and not the baseline, and so the same gain factors appear in many baselines. This redundancy has led to the development of additional off-line procedures to "self-calibrate" radio imaging data using "closure amplitude" techniques (see §5.2.1).

Once the system drifts have been estimated by measurements of the calibrator, this correction can be applied to the whole dataset. Figure 8 shows the calibrated result, where the calibrator flux was assumed to be 30 Jy. In practice, radio phase calibrators are time-variable in flux and so each dataset typically includes an "amplitude calibrator," a well-studied object with known flux as a reference. These calibrated data can now be averaged and used for further model fitting or synthesis imaging. In the example shown here, both the target and calibrator have reasonable signal-to-noise-ratio. In a more realistic case, the signal-to-noise of the target will be orders of magnitude worse – indeed, in one observing block there may be no discernable signal at all! The calibrator measurements are used to phase up the array and allow for very long phase-coherent integrations (averaging in the complex (u,v) plane). Unfortunately, this "blind" phase referencing can not generally be used in optical interferometry (see §3.1.3) where the short atmospheric coherence time and the worse turbulence requires active fringe tracking for both target and calibrator at all times.

Note that actual data will not look quite like this simplified schematic. First, raw data might have random data glitches or bad values that need to be flagged. Also, one tends to only observe the calibrator for a short time, just enough to measure the phase. In fact, the time to slew between targets can be similar to the length of time spent integrating on each calibrator. The time spent on the target during each visit is generally as long as possible given the atmospheric coherence time which can vary greatly with baseline length, observing conditions, and wavelength (see §2.4).

A common complication is that the calibrator may not be an unresolved object nor constant in flux. NRAO maintains a calibrator database that is used to determine the suitability of each calibrator for different situations. As long as the calibrator morphology is known, the observer can apply a visibility amplitude and phase correction to account for the known structure. After this correction, the calibration procedure is the same.

For visible and infrared interferometry, the procedure is very similar. In general, optical interferometers measure a time-averaged squared-visibility and not visibility amplitude since the \mathcal{V}^2 can be bias-corrected more easily for low signal-to-noise ratio data when observing with no phase referencing (Colavita 1999). As discussed earlier, optical interferometers cannot employ phase referencing between two targets¹² due to the tiny isoplanatic patch and short temporal coherence times. Instead of averaging fringe phases, closure phases (see §5.2.1) are formed and averaged over longer time frames following a similar interpolation of calibration data. Lastly, calibrators tend to

¹²Phase referencing is possible using "Dual Star Feeds" which allows truly simultaneous observing of a pair of objects in the same narrow isoplanatic patch on the sky. This capability has been demonstrated on PTI, Keck, and VLTI.

be stars with known or well-estimated diameters. For a given baseline, the observed raw calibrator \mathcal{V}^2 are boosted to account for partially resolving them during the observation before the system visibility is estimated.

When carrying out spectral line and/or polarization measurements, additional calibrations are required. As for single telescope observations, one must observe a source with known spectrum and/or polarization signature in order to correct for system gains. These procedures add steps to the data reduction but are straightforward.

A diversity of packages and data analysis environments are in use for data reduction of interferometer observations. In the radio and mm-wave regime, the most popular packages are AIPS and Miriad. In addition, the CASA package will be used for ALMA and supports many EVLA operations now too. In the visible and infrared, the data reduction packages are usually closely linked to the instrument and are provided by the instrument builders. In most cases there are data analysis “cookbooks” that provide step-by-step examples of how to carry out all steps in the data reduction. Few instruments have complete pipelines that require no user input, although improved scripting is a high priority for future development. A number of summer schools are offered that train new users of interferometer facilities in the details of observation planning and data reduction.

The data products from this stage are calibrated complex visibilities and/or closure phases. No astronomical interpretation has occurred yet. The *de facto* standard data format for radio data is UVFITS. Unfortunately this format is not strictly defined but rather represents the data supported by the NRAO AIPS package and importable into CASA (which uses a new format called the *Measurement Set*). Recently the VLBA community fully documented and registered the FITS Interferometry Data Interchange (FITS-IDI) format (see “*FITS-IDI definition document*” *AIPS Memo 114*). The optical interferometry community saw the problems of radio in having a poorly defined standard and, through IAU-sanctioned activities, crafted a common FITS-based data standard called OIFITS whose specifications were published by Pauls et al. (2005). This standard is in wide use by most optical interferometers in the world today.

4.2. Model-fitting for poor (u,v) coverage

The ultimate goal of most interferometric observations is to have sufficient data quality and (u,v) coverage to make a synthesis image. With high image fidelity, an astronomer can interact with the image just as one would had it come from a standard telescope imager.

Still, cases are plentiful where this ideal situation is not achievable and one will fit a model to the visibility data directly. There are two classes of models: *geometric* models and *physical* models. *Geometric models* are simple shapes that describe the emission but without any physics involved. Common examples include Gaussians, uniform disks, binary system of 2 uniform disks, etc. *Physical models* start with a physical picture including densities, opacities, and sources of energy. Typically a radiative transfer calculation is used to create a synthetic image which can

be Fourier-transformed (following Equation 2) to allow fitting to complex visibilities. Geometric models are useful for very simple cases when an object is marginally resolved or when physical models are not available (or not believable!). Physical models are required to connect observations with “real” quantities like densities and temperatures, although size scales can be extracted with either kind of model.

In radio and mm-wave, model fitting is now relatively rare¹³ since high-fidelity imaging is often achievable. However in the optical, model fitting is still the most common tool for interpreting interferometry data. In many cases, a simple uniform disk or Gaussian is adequate to express the characteristic size scale of an object. By directly fitting to visibility amplitudes, the data can be optimally used and proper error analysis can be performed. The fitting formulae for the two most common functions can be expressed in closed form as a function of baseline B and wavelength λ :

$$|\mathcal{V}| = 2 \frac{J_1(\pi B \Theta_{\text{diameter}}/\lambda)}{\pi B \Theta_{\text{diameter}}/\lambda} \quad \text{case : Uniform Disk} \quad (15)$$

$$|\mathcal{V}| = e^{-\frac{\pi^2}{4 \ln 2} (\Theta_{\text{FWHM}} B/\lambda)^2} \quad \text{case : Gaussian} \quad (16)$$

Figure 9a illustrates both the model-fitting process and the importance of choosing the most physically-plausible function. Here some simulated visibility data spanning baselines from 0 to 60 m are plotted along with curves for 5 common brightness distributions – a uniform disk, a Gaussian disk, two binary models and a ring model. For the case of marginally resolved objects, only the *characteristic scale* of a given model can be constrained and there is no way to distinguish *between models* without longer baseline information (for more elaborate discussion, see Lachaume 2003). Note how all the curves fit the data equally well at short baselines and high visibilities, but that the *interpretation* of each curve is quite different. Without longer baselines that can clearly distinguish between these models, the observer must rely on theoretical expectations to guide model choice. For example a normal G star should closely resemble a uniform disk in the near-infrared while disk emission from a young stellar object in the sub-mm might be more Gaussian. Despite the uncertainties when fitting to marginally resolved targets, fitting interferometric data allows very precise determinations of model parameters as can be seen in Figure 9b where the CHARA Array was used to monitor the variations in diameter of the Cepheid variable δ Cep.

A recently-published example of model-fitting at longer wavelengths is shown in Figure 10. Here, a semi-analytic physical model (in this case of a circumstellar disk) was used to simultaneously fit the spectral energy distribution along with the visibility data. When realistic physical models are available, multi-wavelength constraints can make a dramatic improvement to the power of high angular resolution data and should be included whenever possible.

¹³Historically, model-fitting was the way data was handled in order to discern source structure in the early days of radio interferometry. A classic example is the model of Cygnus A, which Jennison and Das Gupta fitted to long-baseline intensity-interferometry data at 2.4-m wavelength in 1953 (Jennison & Das Gupta 1953). Sullivan (2009, page 353 et. seq) gives more details of this fascinating story.

5. Synthesis imaging

Interferometer data in their raw form are not easy to visualize. Fortunately, as discussed in §2.2, the measured complex visibilities can be transformed into an equivalent brightness distribution on the sky – *an image*. This procedure is called “aperture synthesis imaging” or more generally “synthesis imaging.” In this section, the critical data analysis steps are described for creating an image in both the ideal case as well as more challenging scenarios when faced with poor (u,v) coverage and phase instability.

5.1. Ideal case

Under ideal conditions the astronomer will have collected interferometer data with a large number of telescopes including some Earth rotation to fill-in gaps in (u,v) coverage (see §3.2). In addition, each datum will consist of a fully calibrated complex visibility – both amplitude and phase information. Modern radio arrays such as the VLA and ALMA produce data of this quality when proper phase-referencing procedures (see §3.1.3) are employed.

Figure 11 depicts the Fourier coverage for a 6 telescope interferometer along with the resulting image from a direct Fourier transform of this coverage for a perfect point source (by construction, the image will be purely real). In this procedure, the values in the (u,v) grid are set to unity where data exists and to zero where no data exists. This resulting image shows artifacts because of the missing (u,v) data that were zeroed out. These artifacts are often called “sidelobes” and show both positive and negative excursions – note that negative flux density is usually a strong sign of a sidelobe since negative values in an image are typically unphysical (except for special applications like absorption line studies or polarization stokes mapping). Note that the central core of the image represents the diffraction-limited angular resolution of this observation. Often in a practical situation, the central core will be elongated because (u,v) coverage is not perfectly symmetric, with longer baselines in some directions than others. The last panel in this figure shows the resulting image for a binary star with 2:1 flux ratio. Notice that the image contains two sources, however both sources show the same pattern of artifacts as the simple point source. Indeed, this supports the previous assertion that missing (u,v) coverage is the main origin of this pattern and suggests that the image quality can be improved by correcting for the sidelobe effect.

To proceed, the well-known Convolution Theorem must be introduced: *Multiplication in the “(u,v) space” is equivalent to a convolution in “image space.”* Mathematically, this as can be expressed:

$$\text{FT}(\tilde{\mathcal{V}}(u, v) \cdot M(u, v)) = (\text{FT } \tilde{\mathcal{V}}) \otimes (\text{FT } M) \quad (17)$$

$$\tilde{\mathcal{V}}(u, v) \cdot M(u, v) \Leftrightarrow I(x, y) \otimes B(x, y) \quad (18)$$

where $\tilde{\mathcal{V}}$ is the full underlying complex visibility that could in principle be measured by the interferometer, M is the (u,v) mask that encodes whether data exists (1) or is missing (0)¹⁴, FT and \Leftrightarrow denote a Fourier Transform, $I = \text{FT } \tilde{\mathcal{V}}$ is the true image distribution, and $B = \text{FT } M$ is called the “Convolving Beam.”

Application of the convolution theorem permits an elegant reformulation of the imaging problem into a “deconvolution” problem, where the convolving beam is a complicated function but derived directly from M , the observed (u,v) coverage. Since M is exactly known, the convolving beam B is known as well. Note that this deconvolution problem contrasts sharply with the deconvolution problem in adaptive optics imaging where the point source function (PSF) varies in time and is never precisely known.

5.1.1. CLEAN Algorithm

One of the earliest methods developed for deconvolution was the CLEAN algorithm (Högbom 1974), which is still widely used in radio interferometry. In CLEAN, the Fourier transform of the gridded complex visibility data is called the “dirty image” (or sometimes “dirty map”) and the Fourier transform of the (u,v) plane mask is called the “dirty beam.” One first needs to deconvolve the dirty image with the dirty beam. To do this, the true image I is iteratively constructed by locating the peak in the dirty image and subtracting from this a scaled version of the dirty beam centered at this location. Here, the scaling of the dirty beam is typically tuned to removed a certain fraction of intensity from the peak, often 5%. One keeps track of how much one removes by collecting the “CLEAN” components in a list.

Consider this example. The dirty image has peak of 1.0 Jy at pixel location (3,10). One creates a scaled dirty beam with a peak of 0.05 Jy, shifts the peak to the position (3,10), and subtracts this scaled dirty beam from the dirty image. This CLEAN component is collected and labeled by location (3,10) and flux contribution (0.05 Jy). Continue this procedure, flux is removed from dirty image and CLEAN components are collected. This procedure is halted when the residual dirty image contains only noise. Since the intensity in the true image is expected to be positive-definite, one common criterion for halting the CLEAN cycles is when the largest negative value in the image is comparable to the largest positive value in the image, thereby avoiding any CLEAN components having negative flux.

In principle, this collection of delta function point sources (all the CLEAN components) *is* the best estimate of the image distribution. However, an image of point sources is not visually appealing and a common procedure is to convolve the point source distribution with a “CLEAN” beam, a perfect 2-D Gaussian with a core that matches the FWHM of the dirty beam. Commonly,

¹⁴In general, one can consider a full “Spatial Transfer Function” which can have weights between 0 and 1. Here, consider just a simple binary mask in the (u,v) plane for simplicity.

a filled ellipse will be included in the corner of a CLEANed image showing the 2D FWHM of the restoring beam. Lastly, one adds back the residual image from the dirty map (which should contain only noise) so that the noise level is apparent in the final image and remnant uncorrected sidelobe artifacts, if present, can be readily identified. These steps are illustrated in Figure 12 where the CLEAN procedure has been applied to the examples shown in Figure 11.

The steps of the CLEAN algorithm are summarized below.

1. Create dirty map and beam.
2. Find peak of dirty map.
3. Subtract scaled version of dirty beam from dirty map, removing a small percentage (e.g., $\sim 5\%$) of peak intensity. Collect CLEAN components.
4. Repeat last step until negative residuals are comparable to positive residuals.
5. Convolve CLEAN components with CLEAN beam.
6. Add back the residuals.

While it is beyond the scope to address the weaknesses of the CLEAN algorithm in detail, a few issues are worth mentioning in passing. Typical CLEAN algorithms do not naturally deal with errors unless all the visibility data are of similar quality. The case when each visibility point is weighted equally is called *natural weighting* (which gives best SNR for detecting faint objects) and the case when each portion of the (u,v) plane is equally weighted, so called *uniform weighting* (which gives somewhat higher angular resolution but at some loss of sensitivity). Briggs (1995) introduced a “ROBUST” parameter that can naturally span these two extremes. Other problems with CLEAN include difficulty reconstructing low surface brightness regions, large scale emission and the fact that the final reconstructed image is of a degraded resolution because the convolving PSF actually suppresses the longest baseline visibilities from the final image. Finally, if the imaging step makes use of the Fast Fourier Transform, several additional artifacts can appear in the image as a consequence of the necessity to grid the input u, v data.

5.1.2. Maximum Entropy Method (MEM)

Another common method for reconstructing images from interferometric data is called the *Maximum Entropy Method* (Gull & Skilling 1983; Skilling & Bryan 1984). This approach asks the question: “How to choose which reconstructed image is best, considering that there are an infinite number of images that can fit the interferometer dataset within the statistical uncertainties?” The simple answer here is that the “best” image is the one that both fits the data acceptably and also maximizes the *Entropy* S defined as:

$$S = - \sum_i f_i \ln \frac{f_i}{m_i} \quad (19)$$

where f_i is the (positive-definite) fraction of flux in pixel i , and m_i is called the *image prior* which can encapsulate prior knowledge of the flux distribution (e.g., known from physical considerations or lower resolution observations). Narayan & Nityananda (1986) describe general properties of this algorithm in a lucid review article and motivates the above methodology using *Bayes' Theorem*, the cornerstone of so-called *Bayesian Statistics*.

Entropy is an interesting statistic since it quantifies the amount of complexity in a distribution. It is often stated that MEM tries to find the “smoothest image” consistent with the data. This indeed is a highly desirable feature since any structures in the reconstructed image should be based on the data itself and not artifacts from the reconstruction process. However, MEM does not actually select the smoothest image but rather one with “most equal” uniform set of values – MEM does not explicitly take into account spatial structure but only depends on the distribution of pixel values. Indeed with more study, the Maximum Entropy functional has been found not to be that special, except for its privileged appearance in physics. From a broader perspective, maximum entropy can be considered one member of a class of regularizers that allow the inverse problem to be well-defined, and MEM is not necessarily the best nor even suitable for some imaging problems (e.g., other regularizers include total variation or maximum likelihood).

MEM performs better for reconstructing smooth large scale emission than CLEAN, although MEM is much more computationally demanding. MEM can naturally deal with heterogeneous data with varying errors since the data is essentially fitted using a χ^2 -like statistic. This involves only a “forward” transform from image space to (u,v) space, thus avoiding all the issues of zeros in the (u,v) grid and the need for deconvolution. In addition, MEM images possess *super-resolution* beyond the traditional $\sim \frac{\lambda}{D}$ diffraction limit since smoothness is introduced in the process only indirectly through the Entropy statistic. For instance, if the object is a point-like object, then the FWHM of the reconstructed MEM image depends on the signal-to-noise of the data, not just the length of the longest baseline. Super-resolution is viewed with some skepticism by practitioners of CLEAN because structures beyond the formal diffraction limit may be artifacts of the Entropy functional. MEM has been implemented in many radio interferometry data processing environments, such as AIPS for VLA/VLBA, Caltech VLBI package (Sivia 1987), and for optical interferometry (e.g., BSMEM, Buscher 1994).

5.2. Non-ideal cases for imaging

Most modern interferometric arrays in the radio (VLA) and millimeter (ALMA, CARMA) have a sufficient number of elements for good (u,v) coverage and also employ rapid phase referencing for absolute phase calibration. This allows either CLEAN and MEM methods to make imaging possible, although mosaicing large fields can still pose a computational challenge.

In optical interferometry and perhaps also at some sub-mm wavelengths, atmospheric turbulence changes the fringes phases so quickly and over such small angular scales that phase referencing is not practical. As discussed earlier, modeling can still be done for the visibility amplitudes but the turbulence scrambles the phase information beyond utility. Fortunately, there is a clever method to recover some of the lost phase information and this is discussed next.

5.2.1. Closure Phase, the Bispectrum, and Closure Amplitudes

As discussed earlier, phase referencing is used to correct for drifting phases. So what can be done when phase referencing is not possible? Without valid phase information accompanying the visibility amplitude measurements, one cannot carry out the inverse Fourier Transform that lies at the core of synthesis imaging and the CLEAN algorithm specifically. While in some cases the fringe phases do not carry much information (e.g., for symmetrical objects), in general phases carry most of the information for complex scenes.

Early in the history of radio interferometry a clever idea, now referred to as “closure phase,” was discovered to recover some level of phase information when observing with three telescopes (Jennison 1958). The method was introduced to partly circumvent the combination of poor receiver stability and variable multi-path propagation in early radio-linked long-baseline ($\gtrsim 2$ km) interferometer systems at Jodrell Bank. The term “closure phase” itself appeared later on, in the paper by Rogers et al. (1974) describing an application at centimeter radio wavelengths using very stable and accurate, but independent, reference oscillators at the three stations in a so-called very long baseline interferometer (VLBI) array. Closure phase was critical for VLBI work in the 1980s although it became less necessary as phase referencing became feasible. Application at optical wavelengths was first mentioned by Rogstad (1968), but carried out only much later in the optical range through aperture masking experiments (e.g., Baldwin et al. 1986). By 2006, nearly all separated-element optical arrays with 3 or more elements have succeeded in obtaining closure phase measurements (COAST, NPOI, IOTA, ISI, VLTI, CHARA). An optical observer now can expect closure phases to be a crucial observable for most current instrumentation.

The principle behind the power of closure phases is briefly described and the interested reader is referred to Monnier et al. (2007) for more detailed information on taking advantage of such phase information in optical interferometry.

Consider Figure 13a in which a time delay is introduced above one slit in a Young’s interferometer. This time delay introduces a phase shift for the detected fringe and the magnitude of the phase shift is independent of the baseline length. For the case of 3 telescopes (see Figure 13b), a delay above one telescope will introduce phase shifts in *two fringes*. For instance, a delay above telescope 2 will show up as an equal phase shift for baseline 1-2 and baseline 2-3, but with *opposite* signs. Hence, the sum of three fringe phases, between 1-2, 2-3, and 3-1, will be insensitive to the phase delay above telescope 2. This argument holds for arbitrary phase delays above any of the

three telescopes. In general, the sum of three phases around a closed triangle of baselines, the *closure phase*, is a good interferometric observable; that is, it is independent of telescope-specific phase shifts induced by the atmosphere or optics.

The closure phase Φ_{ijk} can thus be written in terms of the three telescopes i, j, k in the triangle:

$$\Phi_{ijk} = \phi_{ij} + \phi_{jk} + \phi_{ki} \quad (20)$$

where ϕ_{ij} represents the measured Fourier phase for the baseline connecting telescopes i, j . Alternatively, the closure phase can be written in terms of the (u_0, v_0, u_1, v_1) in the Fourier (hyper-)plane where (u_0, v_0) represents the (u, v) coverage for baseline i, j in the triangle, (u_1, v_1) represents the (u, v) coverage for baseline j, k in the triangle, and the last leg of the triangle can be calculated from the others since the sum of the 3 baselines must equal zero to be a “closure triangle.” See definition and explanation put forward in documentation of the OI-FITS data format (Pauls et al. 2005).

Another method to derive the invariance of the closure phase to telescope-specific phase shifts is through the *bispectrum*. The bispectrum $\tilde{B}_{ijk} = \tilde{V}_{ij}\tilde{V}_{jk}\tilde{V}_{ki}$ is formed through triple products of the complex visibilities around a closed triangle, where ijk specifies the three telescopes. Using Eq. 14 and using the concept of telescope-specific complex gains G_i , it can be seen how the telescope-specific errors affect the measured bispectrum:

$$\tilde{B}_{ijk} = \tilde{V}_{ij}^{\text{measured}} \tilde{V}_{jk}^{\text{measured}} \tilde{V}_{ki}^{\text{measured}} \quad (21)$$

$$= |G_i||G_j|e^{i(\Phi_i^G - \Phi_j^G)}\tilde{V}_{ij}^{\text{true}} \cdot |G_j||G_k|e^{i(\Phi_j^G - \Phi_k^G)}\tilde{V}_{jk}^{\text{true}} \cdot |G_k||G_i|e^{i(\Phi_k^G - \Phi_i^G)}\tilde{V}_{ki}^{\text{true}} \quad (22)$$

$$= |G_i|^2|G_j|^2|G_k|^2\tilde{V}_{ij}^{\text{true}} \cdot \tilde{V}_{jk}^{\text{true}} \cdot \tilde{V}_{ki}^{\text{true}} \quad (23)$$

From the above derivation, the bispectrum is a complex quantity whose phase is identical to the closure phase, while the individual telescope gains affect only the bispectrum amplitude. The use of the bispectrum for reconstructing diffraction-limited images from speckle data was developed independently (Weigelt 1977) of the closure phase techniques, and the connection between the approaches elucidated only later (Roddier 1986; Cornwell 1987).

A 3-telescope array with its one triangle can provide a single closure phase measurement, a paltry substitute for the 3 Fourier phases available using phase referencing. However, as one increases the number of elements in the array from 3 telescopes to 7 telescopes, the number of independent closure phases increases dramatically to 15, about 70% of the total 21 Fourier phases available. An array the size of the VLA with 27 antennae is capturing 93% of the phase information. Indeed, imaging of bright objects does not require phase referencing and the VLA can make high quality imaging through closure phases alone. Note that imaging using closure phases alone retains no absolute astrometry information; astrometry requires phase-referencing.

A related quantity useful in radio is the *closure amplitude* (which requires sets of 4 telescopes) and this can be used to compensate for unstable amplifier gains and varying antenna efficiencies

(e.g., Readhead et al. 1980). Closure amplitudes are not practical for current optical interferometers partially because most fringe amplitude variations are not caused by telescope-specific gain changes but rather by changing coherence (e.g., due to changing atmosphere).

Closure phases (and closure amplitudes) can be introduced into the imaging process in a variety of ways. For the CLEAN algorithm, the closure phases can not be directly used because CLEAN requires estimates of the actual Fourier phases in order to carry out a Fourier transform. A clever iterative scheme known as *self-calibration* was described by Readhead & Wilkinson (1978) and Cornwell & Wilkinson (1981) which alternates between a CLEANing stage and a self-calibration stage that estimates Fourier phases from the closure phases and most recent CLEANed image. As for standard CLEAN itself, self-calibration can not naturally deal with errors in the closure phases and closure amplitudes, and thus is recognized as not optimal. That said, self-calibration is still widely used along with CLEAN even in the case of phase referencing to dramatically improve the imaging dynamic range for imaging of and around bright objects.

Closure phases, the bispectrum, and closure amplitudes can be quite naturally incorporated into “forward-transform” image reconstruction schemes such as the Maximum Entropy Method. Recall that MEM basically performs a minimization of a regularizer constrained by some goodness-of-fit to the observed data. Thus, the bispectral quantities can be fitted just like all other observables. That said, the mathematics can be difficult and the program BSMEM (Buscher 1994) was one of the first useful software suitable for optical interferometers that successfully solved this problem in practice. Currently, the optical interferometer community have produced several algorithms to solve this problem, including the Building Block Method (Hofmann & Weigelt 1993), MACIM (Ireland et al. 2006), MIRA (Thiébaud 2008), WISARD (Meimon et al. 2008), and SQUEEZE (Baron et al. 2010). See Malbet et al. (2010) for a description of a recent blind imaging competition between some of these algorithms.

5.3. Astrometry

Astrometry is still a specialized technique within interferometry and a detailed description is beyond the scope of this chapter. Typically, the precise separation between two objects on the sky, the *relative astrometry*, is needed to be known for some purpose, such as a parallax measurement. If both objects are known point-like objects with no asymmetric structure, then the precise knowledge of the baseline geometry can be used, along with detailed measurements of interferometric fringe phase, to estimate their angular separation. In general, the astrometric precision $\Delta\Phi$ on the sky is related to the measured fringe phase SNR as follows:

$$\Delta\Phi \sim \frac{\lambda}{\text{Baseline}} \cdot \frac{1}{\text{SNR}} \quad (24)$$

Hence, if one measures a fringe with a signal-to-noise of 100 (which is quite feasible) then one can determine the relative separation of two sources with a precision 100× smaller than the fringe

spacing. Since VLBI and optical interferometers have fringe spacings of ~ 1 milliarcseconds, this allows for astrometric precision at the 10 *microarcsecond* level allowing parallax measurements at many kiloparsecs and also allows us to take a close look around the black hole at the center of the Galaxy. Unfortunately, at this precision level many systematic effects become critical and knowledge of the absolute baseline vector between telescopes is crucial and demanding. The interested reader should consult specific instruments and recent results for more information (Reid et al. 2009; Muterspaugh et al. 2010, for radio and optical respectively).

6. Concluding remarks

In barely more than 50 years, separated-element interferometry has come to dominate radio telescope design as the science has demanded ever-increasing angular resolution. The addition of more elements to an array has provided improvements both in mapping speed and in sensitivity. The early problems with instability in the electronics were solved years ago by improvements in radio and digital electronics, and it is presently not unusual to routinely achieve interferometer phase stability of order $\lambda/1000$ over time spans of many tens of minutes. Sensitivity improvements by further reductions in receiver temperature are reaching a point of diminishing returns as the remaining contributions from local spillover, the Galactic background, and atmospheric losses come to dominate the equation. Advances in the speed and density of digital solid-state devices are presently driving the development of increased sensitivity, with flexible digital signal processors providing wider bands for continuum observations and high frequency resolution for precision spectroscopy. With the commissioning of the billion-dollar international facility ALMA underway and long-term plans for ambitious arrays at longer wavelengths (SKA, LOFAR), the future of “radio” interferometry is bright and astronomers are eager to take advantage of the new capabilities, especially vast improvements to sensitivity.

The younger field of optical interferometry is still rapidly developing with innovative beam combination, fringe tracking methods and extensions of adaptive optics promising significant improvements in sensitivity for years to come. In the long-run however, the atmosphere poses a fundamental limit to the ultimate astrometric precision and absolute sensitivity for visible and infrared interferometry that can only be properly overcome by placing the telescopes into space or through exploring exotic sites such as Dome A, Antarctica. Currently however, the emphasis of the majority of the scientific community favors ever-larger collecting area in the near- and mid-IR (e.g. JWST) as astronomers reach to ever greater distances and earlier times, rather than higher angular resolution.

Eventually, the limits of diffraction are likely to limit the science return of space telescopes, and the traditional response of building a larger aperture will no longer be affordable. Filled apertures increase in weight and in cost as a power > 1 of the diameter (Bely 2003). For ground-based telescopes, cost $\sim D^{2.6}$. In space, the growth is slower, $\sim D^{1.6}$, although the coefficient of pro-

portionality is much larger¹⁵. Over the last two decades the prospects have become increasingly bleak for building ever larger filled-aperture telescopes within the anticipated space science budgets. Interferometry permits the connection of individual collectors of modest size and cost into truly gigantic space-based constellations with virtually unlimited angular resolution (Allen 2007). Ultimately, the pressure of discovery is likely to make interferometry in space at optical, UV, and IR wavelengths a necessity, just as it did at radio wavelengths more than half a century earlier.

A. Appendix: Current Facilities

Table 4 provides a comprehensive list of existing and planned interferometer facilities. These facilities span the range from “private” instruments, currently available only to their developers, to general purpose instruments. An example of the latter is the Square Kilometer Array; this is a major next-generation facility for radio astronomy being planned by an international consortium, with a Project Office at the Jodrell Bank Observatory in the UK (<http://www.skatelescope.org/>). The location for the SKA has not yet been finalized, but (as of 2011) sites in Australia and South Africa are currently being discussed. Plans for the SKA have spawned several “proof-of-concept” or “pathfinder” instruments which are being designed and built including LOFAR (Europe), MeerKAT (South Africa), ASKAP, MWA, and SKAMP (Australia), and LWA (USA).

Table 5 summarizes the wavelength and angular resolution of currently operating arrays open to the general astronomer. A few of the facilities in this list are still under construction. Figure 14 summarizes the vast wavelength range and angular resolution available using the radio and optical interferometers of the world.

¹⁵It’s interesting to note that at some large-enough diameter, ground-based telescopes are likely to become similar in cost to those in space, especially if one considers life-cycle costs.

Table 4: Alphabetical list of current and planned interferometer arrays.

Acronym	Full Name	Lead Institution(s)	Location
ALMA	Atacama Large Millimeter Array	International/NRAO	Chajnantor, Chile
ATA	Allen Telescope Array	SETI Institute	Hat Creek Radio Observatory, CA, USA
ATCA	Australia Telescope Compact Array	CSIRO/ATNF	Narrabri, Australia
CARMA	Combined Array for Research in Millimeter Astronomy	Caltech, UCB, UChicago, UIUC, UMD	Big Pine, California USA
CHARA	Center for High Angular Resolution Astronomy	Georgia State University	Mt. Wilson, CA, USA
DRAO	Dominion Radio Astrophysical Observatory	Herzberg Institute of Astrophysics	Penticton BC, Canada
EVLA	Expanded Very Large Array	NRAO	New Mexico USA
EVN	The European VLBI Network	International	Europe, UK, US, S. Africa, China, Russia
FASR	Frequency Agile Solar Radiotelescope	National Radio Astronomy Observatory + 6 others	Owens Valley, CA, USA
ISI	Infrared Spatial Interferometer	Univ. California at Berkeley	Mt. Wilson, CA, USA
Keck-I	Keck Interferometer (Keck-I to Keck-II)	NASA-JPL	Mauna Kea, HI, USA
LBTI	Large Binocular Telescope Interferometer	LBT Consortium	Mt. Graham, AZ, USA
LOFAR	Low Frequency ARray	Netherlands Institute for Radio Astronomy - ASTRON	Europe
LWA	Long Wavelength Array	US Naval Research Laboratory	VLA Site, NM, USA
MOST	Molonglo Observatory Synthesis Telescope	School of Physics, Univ. Sydney	Canberra, Australia
MRO	Magdalena Ridge Observatory	Consortium of New Mexico Institutions,	Magdalena Ridge, NM, USA
MWA	Murchison Widefield Array	International/MIT-Haystack	Western Australia
NPOI	Navy Prototype Optical Interferometer	Naval Research Laboratory/ U.S. Naval Observatory	Flagstaff, AZ, USA
OHANA	Optical Hawaiian Array for Nanoradian Astronomy	Consortium (mostly French Institutions), Mauna Kea Observatories, others	Mauna Kea, HI, USA
PdB	Plateau de Bure interferometer	International/IRAM	Plateau de Bure, FR
SKA	Square Kilometer Array	see Appendix A	under study
SMA	Submillimeter Array	Smithsonian Astrophysical Observatory	Mauna Kea, HI, USA
SUSI	Sydney University Stellar Interferometer	Sydney University	Narrabri, Australia
VLBA	Very Long Baseline Array	NRAO	Hawaii to St. Croix, US Virgin Islands
VLT-UT	VLT Interferometer (Unit Telescopes)	European Southern Observatory	Paranal, Chile
VLT-AT	VLT Interferometer (Auxiliary Telescopes)	European Southern Observatory	Paranal, Chile
VERA	VLBI Exploration of Radio Astrometry	Nat. Astron. Obs. Japan (NAOJ)	Japan
VSOP-2	VLBI Space Observatory Programme-2	Japan Aerospace Exploration Agency	Space-Ground VLBI
WSRT	Westerbork Synthesis Radio Telescope	Netherlands Institute for Radio Astronomy - ASTRON	Westerbork, NL

Table 5: Subset of those interferometer arrays from Table 4 which are presently open (or will soon be open) for use by qualified researchers from the general astronomy community. “*” indicates capabilities under development.

Acronym	Telescope		Maximum Baseline	Wavelength Coverage	Observer Resources web page link
	Number	Size (m)			
SUSI	2	0.14	64 (640*) m	0.5–1.0 μ m	http://www.physics.usyd.edu.au/sifa/Main/SUSI
NPOI	6	0.12	64 (> 250*) m	0.57–0.85 μ m	http://www.lowell.edu/npoi/
CHARA	6	1.0	330 m	0.6–2.4 μ m	http://www.chara.gsu.edu/CHARA/
MRO*	~10	~1.5	~350 m	0.6–2.5 μ m	http://www.mro.nmt.edu/Home/index.htm
VLTi	4	1.8 – 8.0	130 (202*) m	1–2.5 μ m, 8–13 μ m	http://www.eso.org/sci/facilities/paranal/telescopes/vlti/
Keck-I	2	10.0	85 m	1.5–4 μ m, 8–13 μ m	Http://planetquest.jpl.nasa.gov/Keck/
LBTi*	2	8.4	23* m	1–20 μ m	http://lbt.as.arizona.edu/
ISI	3	1.65	85 (> 100*) m	8–12 μ m	http://isi.ssl.berkeley.edu/
ALMA*	66	7 – 12	15 km	0.3 mm – 3.6 mm	http://science.nrao.edu/alma/index.shtml
SMA	8	6	500 m	0.4 mm – 1.7 mm	http://www.cfa.harvard.edu/sma/
CARMA	23	3.5 – 10.4	2000 m	1.3, 3, 7 mm	http://www.mmarray.org/
PdB	6	15	760 m	1.3, 2, 3 mm	http://www.iram-institute.org/EN/
VLBA	10	25	8000 km	3 mm – 28 cm	http://science.nrao.edu/vlba/index.shtml
eMERLIN	7	25 – 76	217 km	13 mm – 2 m	http://www.e-merlin.ac.uk/
EVN	27	14 – 305	> 10000 km	7 mm - 90 cm	http://www.evlbi.org/
VERA	4	20	2270 km	7 mm – 1.4 cm	http://veraserver.mtk.nao.ac.jp/index.html
ATCA	6	22	6 km	3 mm – 16 cm	http://www.narrabri.atnf.csiro.au/
EVLA	27	25	27 km	6 mm – 30 cm	http://science.nrao.edu/evla/index.shtml
WSRT	14	25	2700 m	3.5 cm – 2.6 m	http://www.astron.nl/radio-observatory/astronomers/wsrt-astronomers
DRAO	7	9	600 m	21, 74 cm	e-mail: Tom.Landecker@nrc-cnrc.gc.ca
GMRT	30	45	25 km	21 cm – 7.9 m	http://www.gmrt.ncra.tifr.res.in
MOST	64	~ 12	1600 m	36 cm	http://www.physics.usyd.edu.au/sifa/Main/MOST
LOFAR	many	simple	1500 km	1.2 m – 30 m	http://www.astron.nl/radio-observatory/astronomers/lofar-astronomers

We are grateful to the following colleagues for their comments and contributions: W.M. Goss, R.D. Ekers, T.L. Wilson, S. Kraus, M. Zhao, T. ten Brummelaar, A. King, and P. Teuben.

REFERENCES

- Allen, R. J. 2007, *PASP*, 119, 914
- Allen, R. J., Goss, W. M., & van Woerden, H. 1973, *A&A*, 29, 447
- Andrews, S. M., Wilner, D. J., Hughes, A. M., Qi, C., & Dullemond, C. P. 2009, *ApJ*, 700, 1502
- Baade, W. & Minkowski, R. 1954, *ApJ*, 119, 206
- Baldwin, J. E., Beckett, M. G., Boysen, R. C., Burns, D., Buscher, D. F., Cox, G. C., Haniff, C. A., Mackay, C. D., Nightingale, N. S., Rogers, J., Scheuer, P. A. G., Scott, T. R., Tuthill, P. G., Warner, P. J., Wilson, D. M. A., & Wilson, R. W. 1996, *A&A*, 306, L13
- Baldwin, J. E., Haniff, C. A., Mackay, C. D., & Warner, P. J. 1986, *Nature*, 320, 595
- Baron, F., Monnier, J. D., & Kloppenborg, B. 2010, in *Society of Photo-Optical Instrumentation Engineers (SPIE) Conference*, Vol. 7734, *Society of Photo-Optical Instrumentation Engineers (SPIE) Conference Series*
- Bely, P. Y. 2003, *The Design and Construction of Large Optical Telescopes* (Springer)
- Bolton, J. G., Stanley, G. J., & Slee, O. B. 1949, *Nature*, 164, 101
- Bosma, A. 1981a, *AJ*, 86, 1791
- . 1981b, *AJ*, 86, 1825
- Bridle, A. H., Hough, D. H., Lonsdale, C. J., Burns, J. O., & Laing, R. A. 1994, *AJ*, 108, 766
- Briggs, D. S. 1995, in *Bulletin of the American Astronomical Society*, Vol. 27, *American Astronomical Society Meeting Abstracts*, # 112.02
- Buscher, D. F. 1994, in *IAU Symposium*, Vol. 158, *Very High Angular Resolution Imaging*, ed. J. G. Robertson & W. J. Tango, 91
- Carilli, C. L. & Holdaway, M. A. 1999, *Radio Science*, 34, 817
- Cohen, M. H., Cannon, W., Purcell, G. H., Shaffer, D. B., Broderick, J. J., Kellermann, K. I., & Jauncey, D. L. 1971, *ApJ*, 170, 207
- Colavita, M. M. 1999, *PASP*, 111, 111

- Colavita, M. M., Serabyn, E., Millan-Gabet, R., Koresko, C. D., Akeson, R. L., Booth, A. J., Mennesson, B. P., Ragland, S. D., Appleby, E. C., Berkey, B. C., Cooper, A., Crawford, S. L., Creech-Eakman, M. J., Dahl, W., Felizardo, C., Garcia-Gathright, J. I., Gathright, J. T., Herstein, J. S., Hovland, E. E., Hrynevych, M. A., Ligon, E. R., Medeiros, D. W., Moore, J. D., Morrison, D., Paine, C. G., Palmer, D. L., Panteleeva, T., Smith, B., Swain, M. R., Smythe, R. F., Summers, K. R., Tsubota, K., Tyau, C., Vasisht, G., Wetherell, E., Wizinowich, P. L., & Woillez, J. M. 2009, *PASP*, 121, 1120
- Cornwell, T. J. 1987, *A&A*, 180, 269
- Cornwell, T. J. & Wilkinson, P. N. 1981, *MNRAS*, 196, 1067
- Danchi, W. C., Bester, M., Degiacomi, C. G., Greenhill, L. J., & Townes, C. H. 1994, *AJ*, 107, 1469
- Delplancke, F., Derie, F., Lév”que, S., Ménardi, S., Abuter, R., Andolfato, L., Ballester, P., de Jong, J., Di Lieto, N., Duhoux, P., Frahm, R., Gitton, P., Glindemann, A., Palsa, R., Puech, F., Sahlmann, J., Schuhler, N., Duc, T. P., Valat, B., & Wallander, A. 2006, in *Society of Photo-Optical Instrumentation Engineers (SPIE) Conference*, Vol. 6268, *Society of Photo-Optical Instrumentation Engineers (SPIE) Conference Series*
- di Benedetto, G. P. & Rabbia, Y. 1987, *A&A*, 188, 114
- Fried, D. L. 1965, *J. Opt. Soc. Am.*, 55, 1427
- Glindemann, A. 2010, *Principles of Stellar Interferometry* (Springer-Verlag)
- Golay, M. 1971, *J. Opt. Soc. Am.*, 61, 272
- Goss, W. M., Brown, R. L., & Lo, K. Y. 2003, *Astronomische Nachrichten Supplement*, 324, 497
- Greenhill, L. J., Gwinn, C. R., Schwartz, C., Moran, J. M., & Diamond, P. J. 1998, *Nature*, 396, 650
- Gull, S. F. & Skilling, J. 1983, in *Indirect Imaging. Measurement and Processing for Indirect Imaging. Proceedings of an International Symposium held in Sydney, Australia, August 30-September 2, 1983*. Editor, J.A. Roberts; Publisher, Cambridge University Press, 267
- Hanbury Brown, R., Davis, J., & Allen, L. R. 1974, *MNRAS*, 167, 121
- Hecht, E. 2002, *Optics* (Boston: Addison-Wesley)
- Heffner, H. 1962, *Proc. IRE*, 50, 1604
- Hofmann, K. & Weigelt, G. 1993, *A&A*, 278, 328
- Högbom, J. A. 1974, *A&AS*, 15, 417

- Holdaway, M. A. & Helfer, T. T. 1999, in *Astronomical Society of the Pacific Conference Series*, Vol. 180, *Synthesis Imaging in Radio Astronomy II*, ed. G. B. Taylor, C. L. Carilli, & R. A. Perley, 537
- Ireland, M. J., Monnier, J. D., & Thureau, N. 2006, in *Society of Photo-Optical Instrumentation Engineers (SPIE) Conference*, Vol. 6268, *Advances in Stellar Interferometry*. Edited by Monnier, John D.; Schöller, Markus; Danchi, William C.. *Proceedings of the SPIE*, Volume 6268, pp. 62681T (2006).
- Jennison, R. C. 1958, *MNRAS*, 118, 276
- Jennison, R. C. & Das Gupta, M. K. 1953, *Nature*, 172, 996
- Johnson, M. A., Betz, A. L., & Townes, C. H. 1974, *Physical Review Letters*, 33, 1617
- Keto, E. 1997, *ApJ*, 475, 843
- Kishimoto, M., Hönl, S. F., Antonucci, R., Kotani, T., Barvainis, R., Tristram, K. R. W., & Weigelt, G. 2009, *A&A*, 507, L57
- Kraus, S., Hofmann, K., Benisty, M., Berger, J., Chesneau, O., Isella, A., Malbet, F., Meilland, A., Nardetto, N., Natta, A., Preibisch, T., Schertl, D., Smith, M., Stee, P., Tatulli, E., Testi, L., & Weigelt, G. 2008, *A&A*, 489, 1157
- Labeyrie, A. 1975, *ApJ*, 196, L71
- Labeyrie, A., Lipson, S. G., & Nisenson, P. 2006, *An Introduction to Optical Stellar Interferometry* (Cambridge University Press)
- Lachaume, R. 2003, *A&A*, 400, 795
- Lane, B. F., Kuchner, M. J., Boden, A. F., Creech-Eakman, M., & Kulkarni, S. R. 2000, *Nature*, 407, 485
- Lawson, P. R., ed. 2000, *Principles of Long Baseline Stellar Interferometry*
- Malbet, F., Cotton, W., Duvert, G., Lawson, P., Chiavassa, A., Young, J., Baron, F., Buscher, D., Rengaswamy, S., Kloppenborg, B., Vannier, M., & Mugnier, L. 2010, in *Society of Photo-Optical Instrumentation Engineers (SPIE) Conference*, Vol. 7734, *Society of Photo-Optical Instrumentation Engineers (SPIE) Conference Series*
- Malbet, F. & Perrin, G., eds. 2007, *Proceedings of the Euro Summer School "Observation and Data Reduction with the VLT Interferometer"* (*New Astronomy Reviews*), Vol. 51, 563–564
- McCready, L. L., Pawsey, J. L., & Payne-Scott, R. 1947, *Royal Society of London Proceedings Series A*, 190, 357

- Meimon, S., Mugnier, L. M., & Le Besnerais, G. 2008, *Journal of the Optical Society of America A*, 26, 108
- Mérand, A., Kervella, P., Coudé du Foresto, V., Ridgway, S. T., Aufdenberg, J. P., ten Brummelaar, T. A., Berger, D. H., Sturmman, J., Sturmman, L., Turner, N. H., & McAlister, H. A. 2005, *A&A*, 438, L9
- Michelson, A. A. & Pease, F. G. 1921, *ApJ*, 53, 249
- Millan-Gabet, R., Schloerb, F. P., & Traub, W. A. 2001, *ApJ*, 546, 358
- Miyoshi, M., Moran, J., Herrnstein, J., Greenhill, L., Nakai, N., Diamond, P., & Inoue, M. 1995, *Nature*, 373, 127
- Monnier, J. D. 2003, *Reports on Progress in Physics*, 66, 789
- Monnier, J. D., Berger, J.-P., Millan-Gabet, R., Traub, W. A., Schloerb, F. P., Pedretti, E., Benisty, M., Carleton, N. P., Hagenauer, P., Kern, P., Labeye, P., Lacasse, M. G., Malbet, F., Perraut, K., Pearlman, M., & Zhao, M. 2006, *ApJ*, 647, 444
- Monnier, J. D., Zhao, M., Pedretti, E., Thureau, N., , M., Muirhead, P., Berger, J., Millan-Gabet, R., Van Belle, G., ten Brummelaar, T., McAlister, H., Ridgway, S., Turner, N., Sturmman, L., Sturmman, J., & Berger, D. 2007, *Science*, 317, 342
- Muterspaugh, M. W., Lane, B. F., Kulkarni, S. R., Konacki, M., Burke, B. F., Colavita, M. M., Shao, M., Wiktorowicz, S. J., & O’Connell, J. 2010, *AJ*, 140, 1579
- Narayan, R. & Nityananda, R. 1986, *ARA&A*, 24, 127
- Oliver, B. M. 1965, *Proc. IEEE*, 53, 436
- Pathria, R. K. 1972, *Statistical Mechanics* (Pergamon Press)
- Pauls, T. A., Young, J. S., Cotton, W. D., & Monnier, J. D. 2005, *PASP*, 117, 1255
- Pawsey, J. L., Payne-Scott, R., & McCready, L. L. 1946, *Nature*, 157, 158
- Peterson, D. M., Hummel, C. A., Pauls, T. A., Armstrong, J. T., Benson, J. A., Gilbreath, G. C., Hindsley, R. B., Hutter, D. J., Johnston, K. J., Mozurkewich, D., & Schmitt, H. R. 2006, *Nature*, 440, 896
- Porcas, R. W., Booth, R. S., Browne, I. W. A., Walsh, D., & Wilkinson, P. N. 1979, *Nature*, 282, 385
- Quirrenbach, A. 2000, in *Principles of Long Baseline Stellar Interferometry*, 71
- Quirrenbach, A. 2001, *ARA&A*, 39, 353

- Quirrenbach, A., Bjorkman, K. S., Bjorkman, J. E., Hummel, C. A., Buscher, D. F., Armstrong, J. T., Mozurkewich, D., Elias, II, N. M., & Babler, B. L. 1997, *ApJ*, 479, 477
- Readhead, A., Nakajima, T., Pearson, T., Neugebauer, G., Oke, J., & Sargent, W. 1988, *AJ*, 95, 1278
- Readhead, A. C. S., Walker, R. C., Pearson, T. J., & Cohen, M. H. 1980, *Nature*, 285, 137
- Readhead, A. C. S. & Wilkinson, P. N. 1978, *ApJ*, 223, 25
- Reid, M. J., Menten, K. M., Brunthaler, A., Zheng, X. W., Moscadelli, L., & Xu, Y. 2009, *ApJ*, 693, 397
- Roddir, F. 1986, *Optics Communications*, 60, 145
- Rogers, A. E. E., Hinteregger, H. F., Whitney, A. R., Counselman, C. C., Shapiro, I. I., Wittels, J. J., Klemperer, W. K., Warnock, W. W., Clark, T. A., & Hutton, L. K. 1974, *ApJ*, 193, 293
- Rogstad, D. H. 1968, *Applied Optics*, 7, 585+
- Rogstad, D. H. & Shostak, G. S. 1972, *ApJ*, 176, 315
- Rots, A. H. 1975, *A&A*, 45, 43
- Rots, A. H. & Shane, W. W. 1975, *A&A*, 45, 25
- Saha, S. K. 2011, *Aperture Synthesis* (Springer)
- Shao, M. & Colavita, M. M. 1992, *A&A*, 262, 353
- Sivia, D. 1987, PhD thesis, Cambridge University
- Skilling, J. & Bryan, R. K. 1984, *MNRAS*, 211, 111
- Smith, F. G. 1951, *Nature*, 168, 555
- Sullivan, W. T. 2009, *Cosmic Noise* (Cambridge: Cambridge University Press)
- Sutton, E. C. & Hueckstaedt, R. M. 1996, *A&AS*, 119, 559
- Taylor, G. B., Carilli, C. L., & Perley, R. A., eds. 1999, *Astronomical Society of the Pacific Conference Series*, Vol. 180, *Synthesis Imaging in Radio Astronomy II*
- ten Brummelaar, T. A., McAlister, H. A., Ridgway, S. T., Bagnuolo, Jr., W. G., Turner, N. H., Sturmman, L., Sturmman, J., Berger, D. H., Ogden, C. E., Cadman, R., Hartkopf, W. I., Hopper, C. H., & Shure, M. A. 2005, *ApJ*, 628, 453

- Thiébaud, E. 2008, in Society of Photo-Optical Instrumentation Engineers (SPIE) Conference, Vol. 7013, Society of Photo-Optical Instrumentation Engineers (SPIE) Conference Series
- Thompson, A. R., Clark, B. G., Wade, C. M., & Napier, P. J. 1980, *ApJS*, 44, 151
- Thompson, A. R., Moran, J. M., & Swenson, Jr., G. W. 2001, *Interferometry and Synthesis in Radio Astronomy*, 2nd Edition (Wiley-Interscience)
- van Boekel, R., Min, M., Leinert, C., Waters, L. B. F. M., Richichi, A., Chesneau, O., Dominik, C., Jaffe, W., Dutrey, A., Graser, U., Henning, T., de Jong, J., Köhler, R., de Koter, A., Lopez, B., Malbet, F., Morel, S., Paresce, F., Perrin, G., Preibisch, T., Przygodda, F., Schöller, M., & Wittkowski, M. 2004, *Nature*, 432, 479
- Visser, H. C. D. 1980a, *A&A*, 88, 159
- . 1980b, *A&A*, 88, 149
- Walsh, D., Carswell, R. F., & Weymann, R. J. 1979, *Nature*, 279, 381
- Weigelt, G. P. 1977, *Optics Communications*, 21, 55
- Whitney, A. R., Shapiro, I. I., Rogers, A. E. E., Robertson, D. S., Knight, C. A., Clark, T. A., Goldstein, R. M., Marandino, G. E., & Vandenberg, N. R. 1971, *Science*, 173, 225
- Wiedner, M. C., Hills, R. E., Carlstrom, J. E., & Lay, O. P. 2001, *ApJ*, 553, 1036
- Wilkinson, P. N., Kellermann, K. I., Ekers, R. D., Cordes, J. M., & Lazio, T. J. W. 2004, *New A Rev.*, 48, 1551
- Willez, J., Akeson, R., Colavita, M., Eisner, J., Ghez, A., Graham, J., Hillenbrand, L., Millan-Gabet, R., Monnier, J., Pott, J., Ragland, S., Wizinowich, P., Appleby, E., Berkey, B., Cooper, A., Felizardo, C., Herstein, J., Hrynevych, M., Martin, O., Medeiros, D., Morrison, D., Panteleeva, T., Smith, B., Summers, K., Tsubota, K., Tyau, C., & Wetherell, E. 2010, in Society of Photo-Optical Instrumentation Engineers (SPIE) Conference, Vol. 7734, Society of Photo-Optical Instrumentation Engineers (SPIE) Conference Series
- Woolf, N. J. 1982, *ARA&A*, 20, 367
- Zhao, M., Monnier, J. D., Pedretti, E., Thureau, N., Mérand, A., ten Brummelaar, T., McAlister, H., Ridgway, S. T., Turner, N., Sturmman, J., Sturmman, L., Goldfinger, P. J., & Farrington, C. 2009, *ApJ*, 701, 209

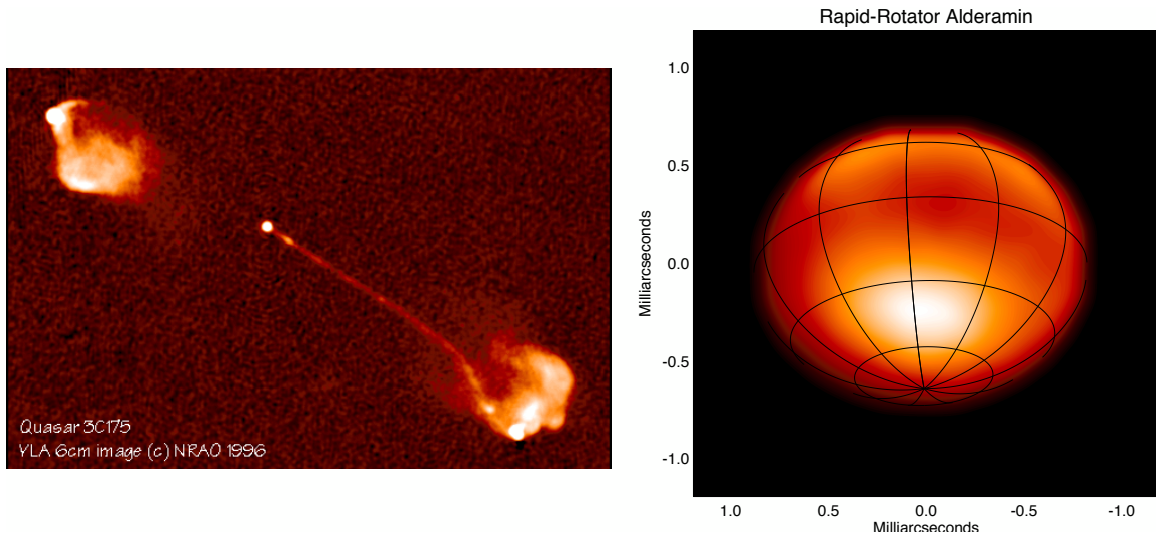


Fig. 1.— Examples of imaging with interferometric arrays. (left) Radio image of jets in quasar 3C175 produced by the Very Large Array with field of view ~ 1 arcminute ~ 200 kpc and angular resolution of 0.35 arcseconds (reprinted with permission Bridle et al. 1994). (right) Near-infrared image of the rapidly-rotating star Alderamin produced by the CHARA Array with field of view of $7 R_{\odot} \sim 2.5$ milli-arcseconds and angular resolution of 0.6 milliarcseconds (reprinted with permission Zhao et al. 2009). The hot polar region and the cool equator is caused by the effect of “gravity darkening.”

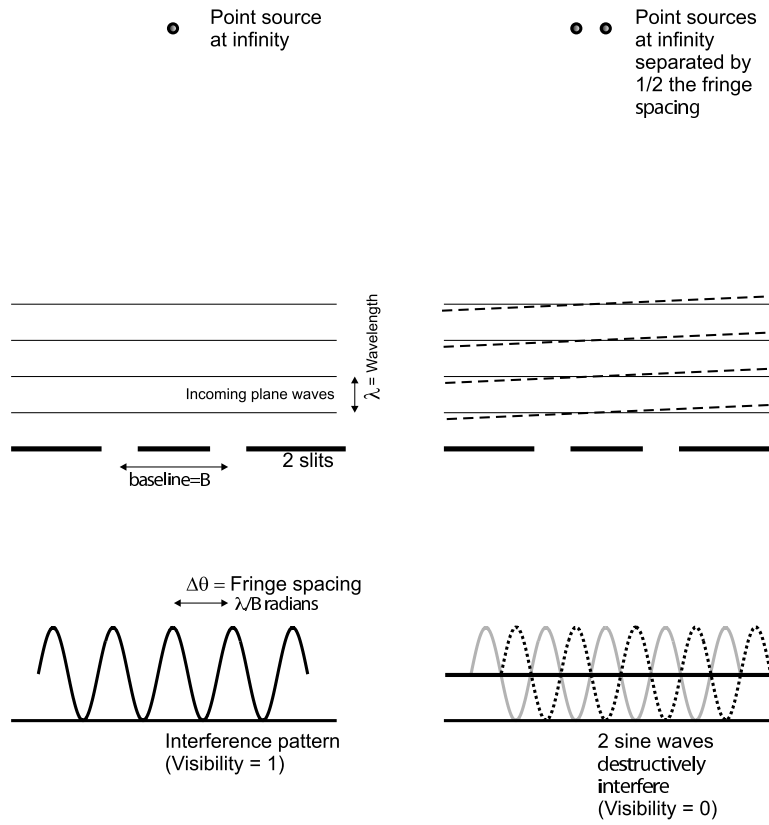


Fig. 2.— Basic operating principle behind interferometry as illustrated by Young's two-slit experiment (adapted from Monnier 2003).

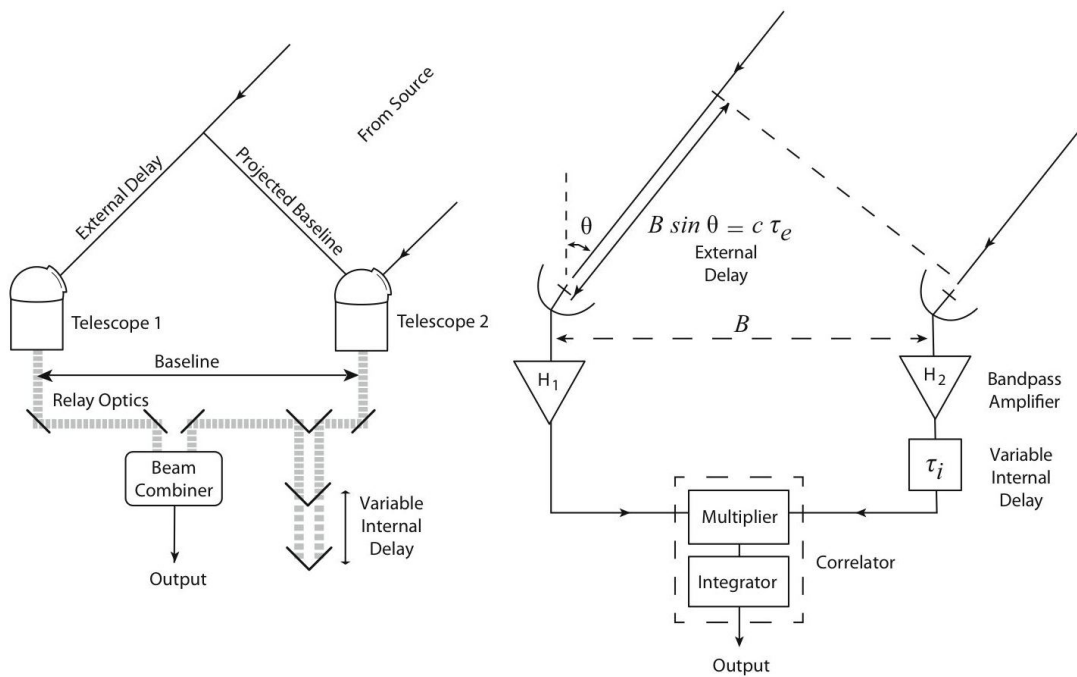


Fig. 3.— Here are more realistic examples of long-baseline interferometers, both optical and radio, including the light collectors and delay line. Left panel: Optical interferometer, adapted from Monnier (2003). Right panel: Radio interferometer, adapted from Figure 2.3 in Thompson et al. (2001). See text for further discussion.

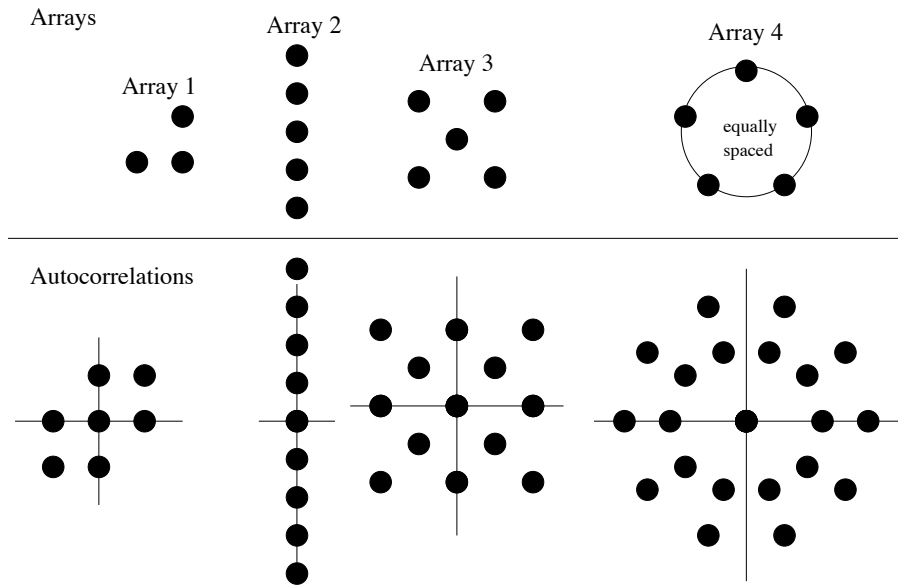


Fig. 4.— Here the “snapshot” coverages of a few simple interferometer layouts are shown for an object located at zenith. The top portion shows the physical layout of 4 examples arrays while the bottom portion shows the corresponding autocorrelation function, which is the same as the (u,v) coverage.

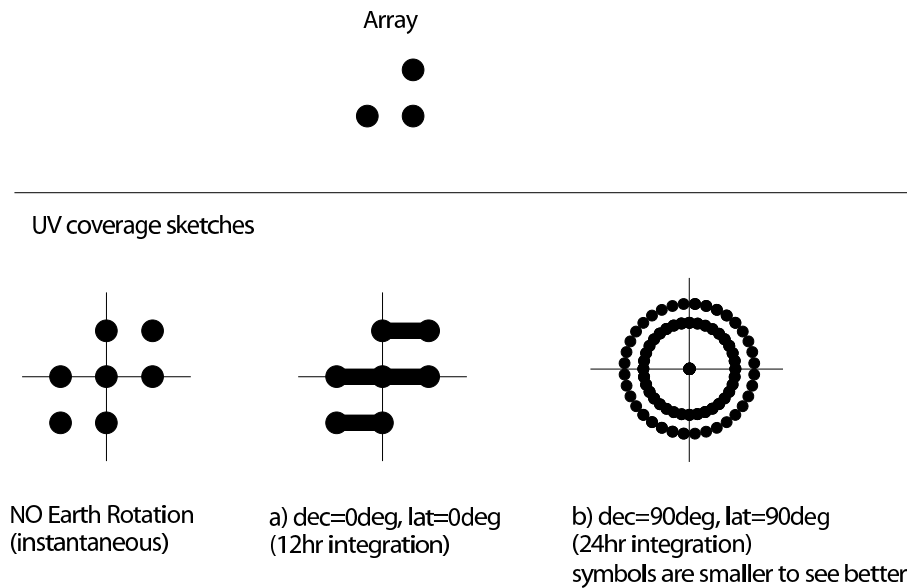


Fig. 5.— The rotation of the Earth introduces changing baseline projections as an object traverses the sky. This figure take a simple 3-telescope array and shows the “ (u,v) tracks” for a few different examples of differing observatory latitudes and target declinations.

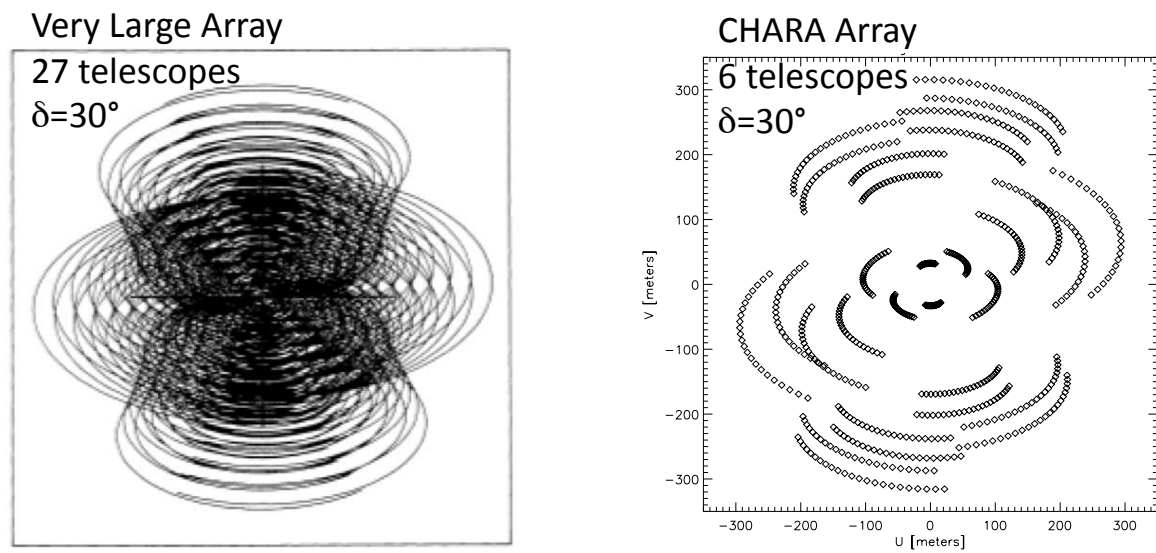


Fig. 6.— This figure shows the dramatic advantage in Fourier coverage that the Very Large Array (VLA) possesses (left panel) compared to the CHARA array (right panel). The radio interferometer VLA, located in Socorro, NM, has 27 (movable) elements and the coverage shown here corresponds to observations ± 4.5 hours around source transit (adapted from Thompson et al. 1980). The optical interferometer CHARA, located on Mt. Wilson, CA, has 6 (fixed) elements and the coverage shown here corresponds to ± 3 hours from transit (adapted from ten Brummelaar et al. 2005). The large gaps in Fourier coverage for CHARA limit its ability to reconstruct highly complex images.

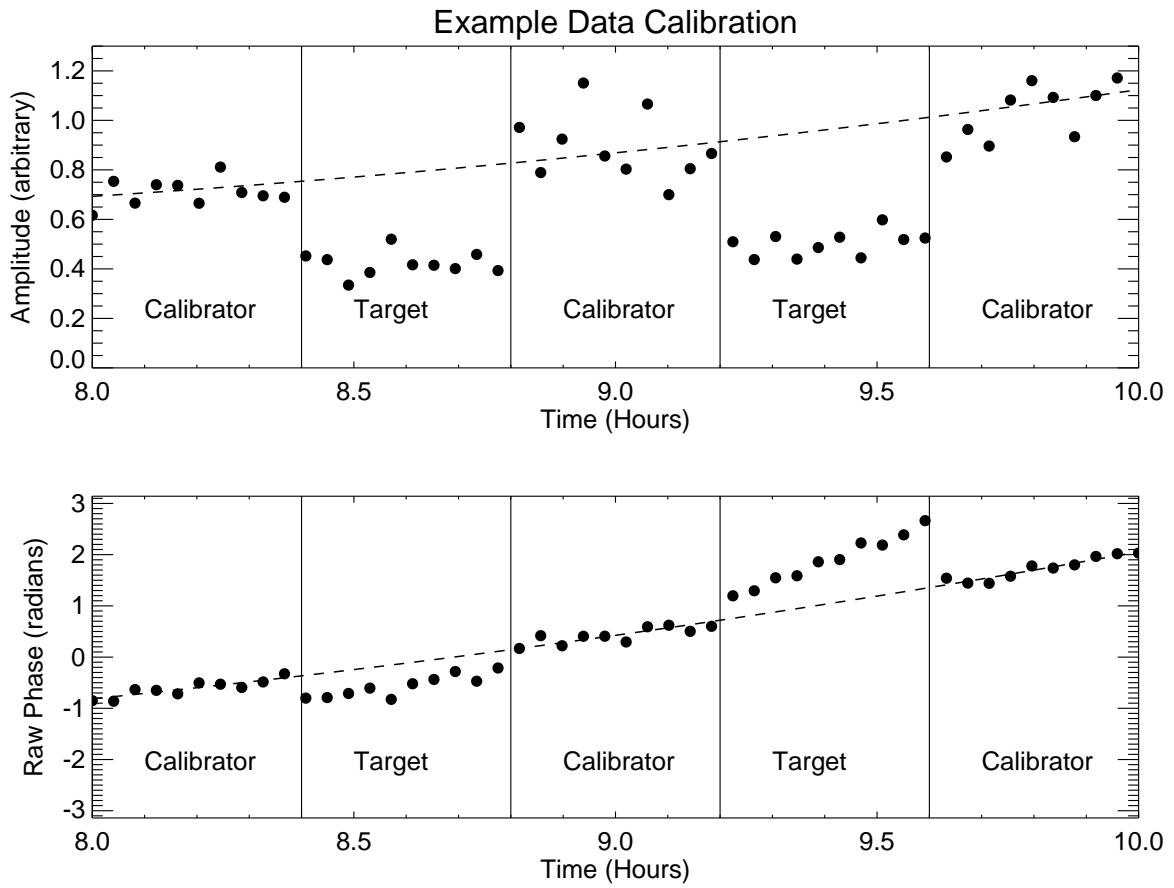


Fig. 7.— First Step of Data Reduction

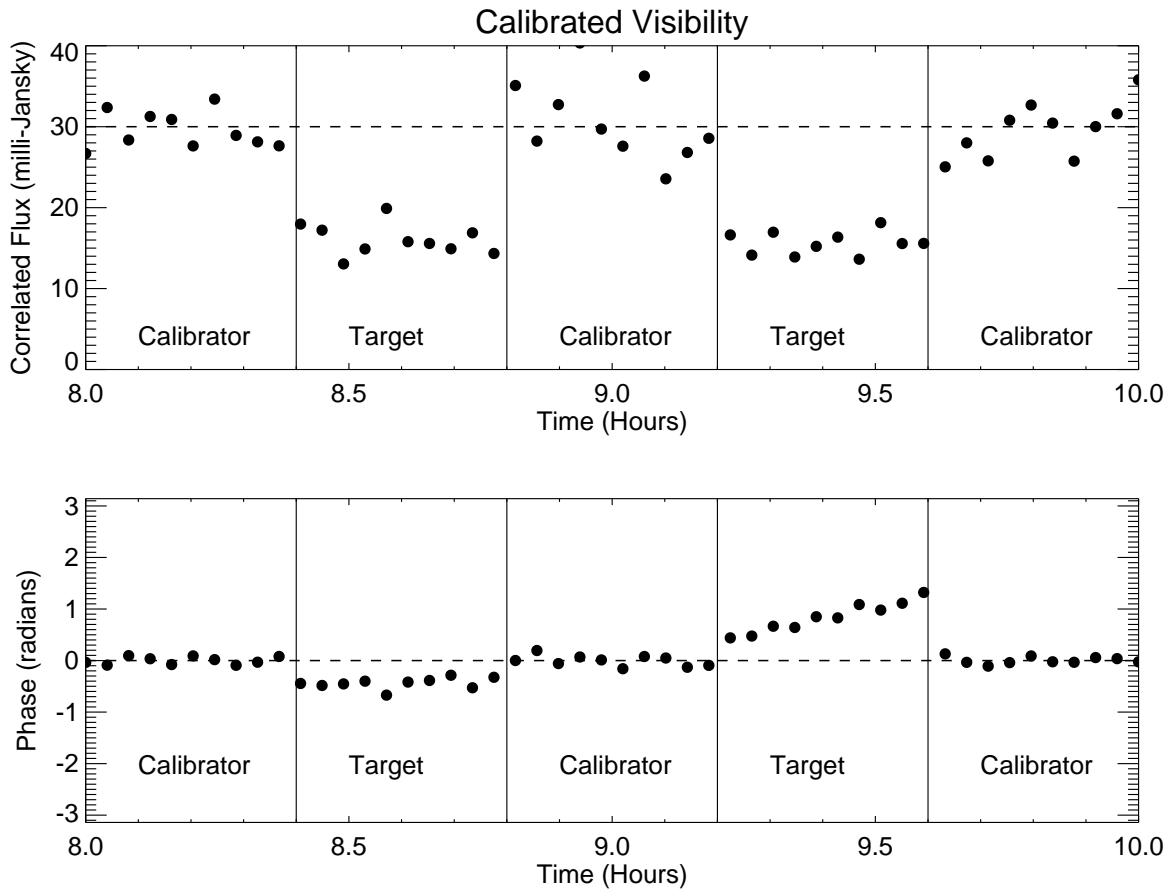


Fig. 8.— Calibrator data following estimate of time-varying system visibilities.

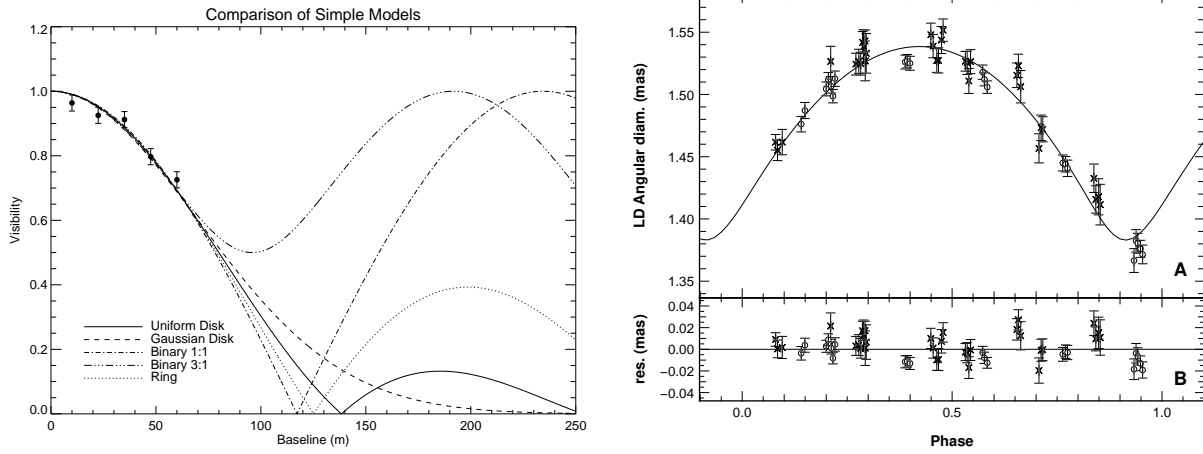


Fig. 9.— (a) This figure shows visibility data and model fits for various brightness distributions, including uniform disk, Gaussian disk, binary system and ring. Notice that all the models fit the data nearly identically for visibility about 50%, corresponding here to baselines shorter than 50 m. One *requires* long baselines (or exceedingly high signal-to-noise ratios) to distinguish between any of these various models, illustrating the importance of *a priori* knowledge of the nature of the target before deciding on appropriate geometrical model description. This figure essentially illustrates in Fourier Space the common sense idea that blurry objects all look the same unless the source structure is larger than the blur – here, longer baselines essentially reduce the blur of diffraction. (b) The right panel shows precision limb-darkened (LD) diameter measurements of the classical Cepheid δ Cep at K band through a full pulsational cycle. These tiny ($\pm 4\%$) changes were easily tracked by the FLUOR combiner at CHARA using ~ 250 - 300 m baselines (reprinted with permission, Mérand et al. 2005).

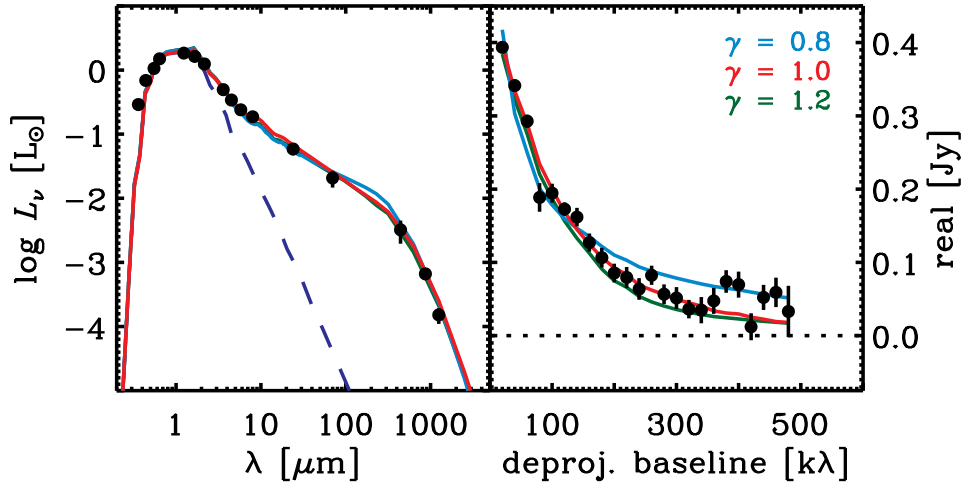


Fig. 10.— This figure illustrates how one can fit spectral energy distributions and visibility simultaneously using simple physical models, as opposed to using purely descriptive or geometric models. Models for protoplanetary disk emission with various radial mass density profiles (left panel) are represented by different colored lines. The visibility data (right panel) were obtained using the Submillimeter Array at 0.87 mm (reprinted with permission, Andrews et al. 2009).

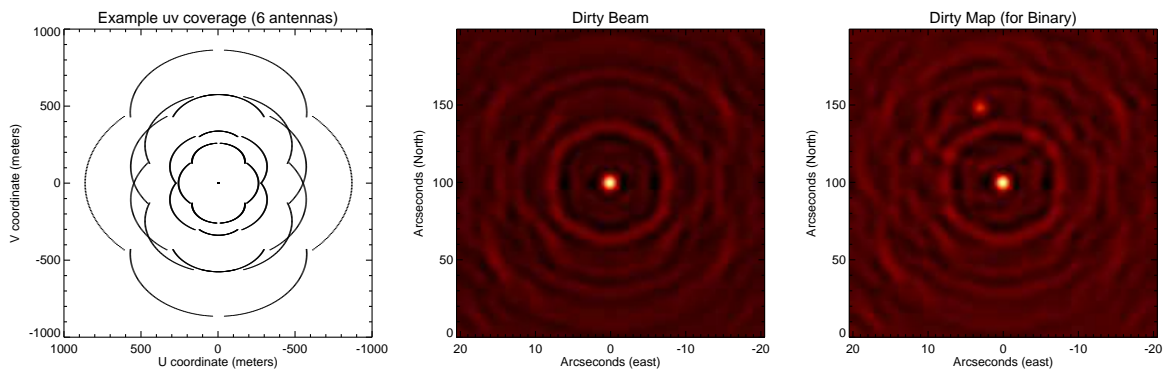


Fig. 11.— The basic elements of the CLEAN algorithm consists of (a) the (u,v) coverage of the observations, (b) the Dirty beam made from the Fourier Transform of the gridded (u,v) support, and (c) the Dirty Map made from Fourier Transform of the observed (u,v) plane.

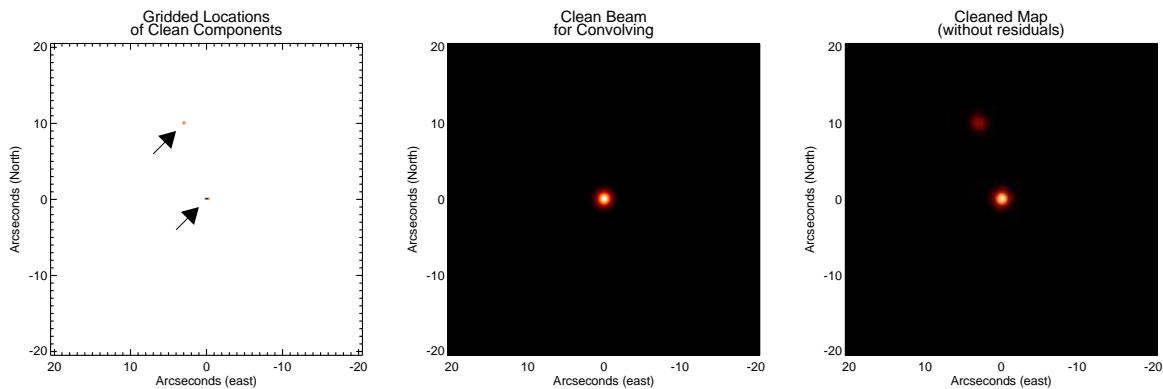


Fig. 12.— The basic “restoration” steps of the CLEAN algorithm consist of (a) collecting the locations of the CLEAN components, (b) creating a CLEAN beam which is a Gaussian beam with same angular resolution of the central portion of the Dirty Beam, and (c) convolving the CLEAN components with the CLEAN beam. Here, the final step of adding back the residuals of the dirty map has been left off. The arrows in panel (a) mark the location of the two clusters of clean components near the locations of the two components of the binary.

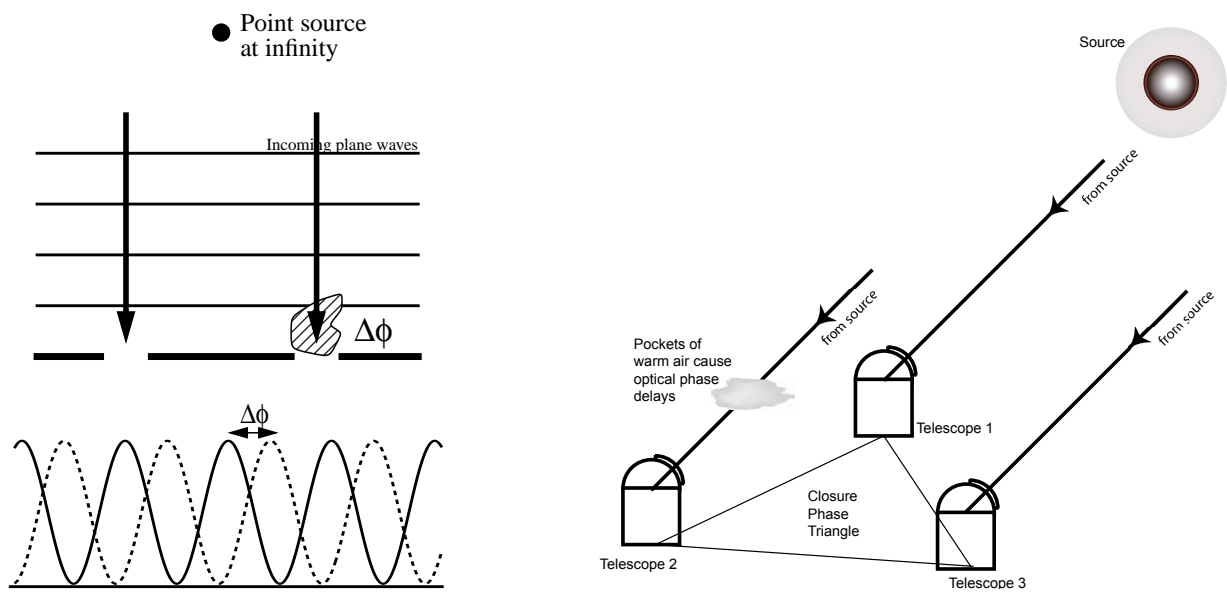


Fig. 13.— (left) Atmospheric turbulence introduces extra path length fluctuations that induce fringe phase shifts. At optical wavelengths, these phase shifts vary by many radians over short time scales ($\ll 1$ sec) effectively scrambling the Fourier phase information. (right) Phase errors introduced at any telescope causes equal but opposite phase shifts in adjoining baselines, canceling out in the *closure phase* (see also Readhead et al. 1988; Monnier et al. 2006). (figures reprinted from Monnier 2003)

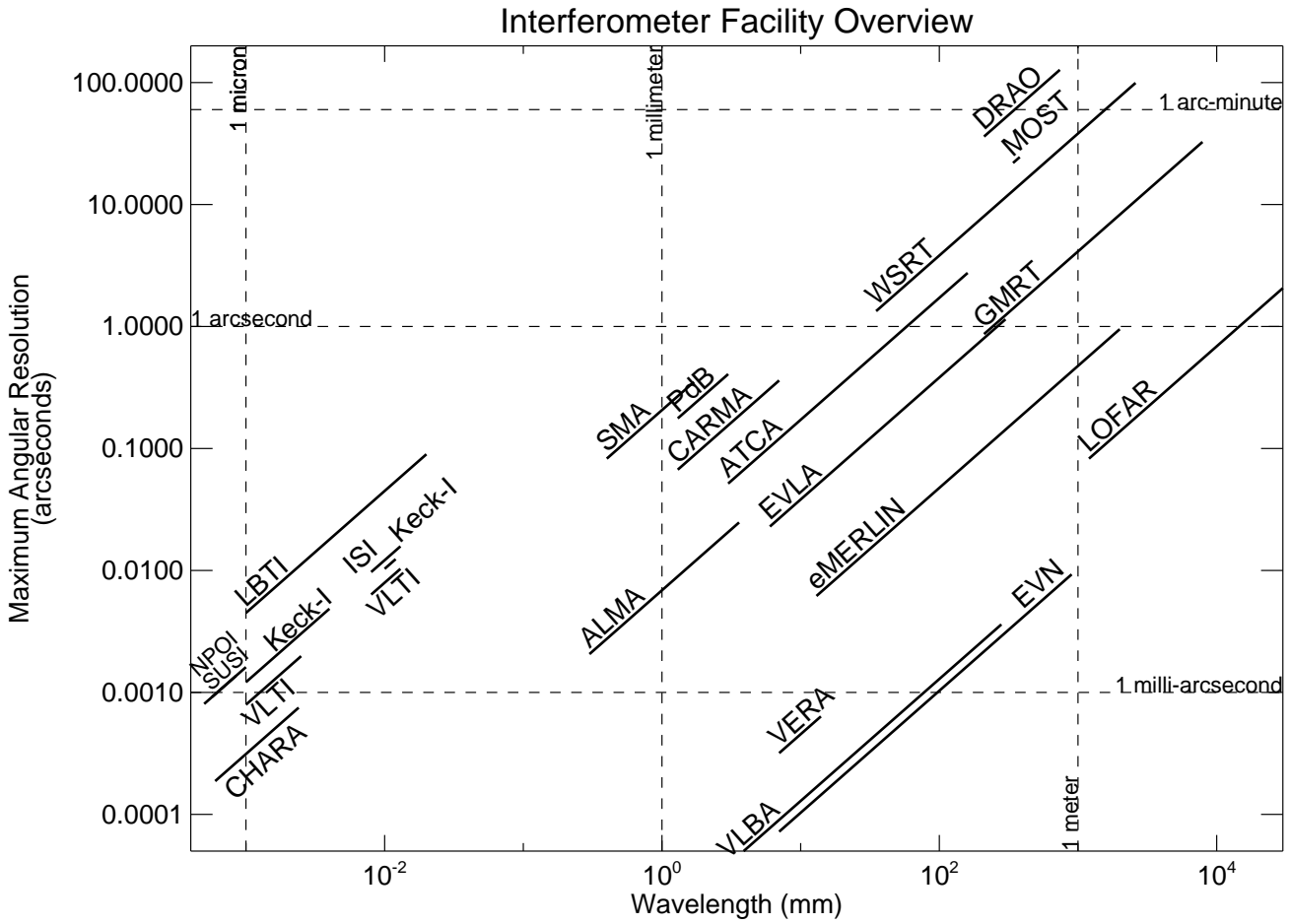


Fig. 14.— Graphical representation of the wavelength coverage and maximum angular resolution available using the radio and optical interferometers of the world. See Table 5 for more information.